UCLouvain

epl

École polytechnique de Louvain

Metal powder as an energy carrier

Experimental setup development for iron combustion assessment

Author: **Hugo PERES**
Supervisors: **Francesco CONTINO, Azd ZAYOUD**
Readers: **Francesco CONTINO, Azd ZAYOUD, Pascal JACQUES**
Academic year 2021–2022
Master [120] in Mechanical Engineering

This page intentionally left blank

Abstract

In a context of energy transition, the use of renewable energy will increase significantly in the next decades. But renewable energy generation and energy demand fluctuate greatly and there can be large excesses of production. It is then of major importance to find ways to store this surplus of energy, and be able to use it whenever it is needed. The present work introduces metal powders as an energy carrier. Indeed, metals in powder form are highly reactive and can burn with air, without emitting GHGs. The solid metal oxide combustion products can then be regenerated via reductions reactions using excess clean energy and be burned again, thus closing a sustainable cycle. Metals have an energy density which is comparable to hydrocarbons, are safe to transport and store, which make them potential candidates to replace fossil fuels in some applications where other means of energy storage such as batteries and hydrogen are not suitable. They can be useful for building or process heating, used in big transportation or help retrofitting coal power plant.

A state of the art on metal powder combustion have been conducted with an attempt in gathering relevant information from different experimental and theoretical studies. The main particularity of metal particles burning is that they burn heterogeneously and after igniting in a kinetic-limited regime, metal particles react in individual diffusion-limited micro-reactor that will lead to their unique appearance of *flames within the flame* combustion front structure.

A setup for burning iron powder has been designed and manufactured in-house. The burner can produce a flame from 3 to 5kW while being able to modify the equivalence ratio of the mixture. The iron particles are fluidized using a 3D-printed feeder, and the mixture is ignited using a pilot propane annular flame. The combustion efficiency was found to be $\geqslant 96\%$.

A critical discussion has been conducted on the use of the designed burner to perform studies. The pilot flame was observed to have a large influence on the proportion of unburned particles. Exhaust gas analysis showed that no NO_x emissions were detected. Observations on solid combustion products showed the formation of larger oxide particles than the initial particle size, indicating that iron do not evaporate during combustion. The work conducted on metal powder combustion is considered a success as the first investigation of metal combustion at UCLouvain for the use of metal powder as energy carrier, and opens a lot of perspectives for the continuity of the metal powder combustion research work.

Acknowledgements

First, I would like to express my gratitude to my thesis supervisor, Prof. Francesco Contino, for giving me the opportunity to perform my master thesis on such an interesting subject, as well as for his valuable comments through the year.

I would like to express my deepest appreciation to my mentor Dr. Azd Zayoud, for supporting and guiding me all along the thesis, which could have not be possible without him.

In addition, I would like to thank all members of the CREDEM technical team for their availability and sympathy. I also thank Pascal Jacques for accepting the task of reader and member of the jury.

Finally, as this marks the end of my studies, I would like to thank warmly my friends and family, for all the moment of joy, their support, during the writing of this thesis and those last years.

Contents

Introduction 1

1 Context and Motivation 2
- 1.1 Energy and climate crisis . . . 2
- 1.2 Power-to-X-to-Power . . . 3
- 1.3 Metal powder as energy carrier . . . 5
  - 1.3.1 Metal candidates . . . 6
  - 1.3.2 Oxidation and reduction processes . . . 7
  - 1.3.3 Real life applications of metal powders as energy carrier . . . 8

2 Metal powder combustion state of the art 11
- 2.1 Experimental setups . . . 11
- 2.2 Metal powder combustion theory . . . 16
  - 2.2.1 Heterogeneous flame . . . 16
  - 2.2.2 Fundamentals on metal powder combustion . . . 17
    - 2.2.2.1 Combustion regime and ignition . . . 18
    - 2.2.2.2 Diffusion-limited combustion modes . . . 24
  - 2.2.3 Influence of input parameters on metal combustion properties 26
    - 2.2.3.1 Burn time . . . 26
    - 2.2.3.2 Flame speed and Burning Velocity . . . 30
    - 2.2.3.3 Particle and gas temperature in diffusion-limited regime . . . 33
    - 2.2.3.4 NO_x emissions . . . 34

3 Experimental design of an iron combustion setup 40
- 3.1 Air and iron flowrates . . . 40
- 3.2 Airflow system . . . 42
- 3.3 Feeding system . . . 42
  - 3.3.1 A word on fluidization theory . . . 42
    - 3.3.1.1 Terminal velocity of a particle . . . 43
    - 3.3.1.2 Particle classification . . . 44

3.3.2 Feeding system state of the art . . . 46
3.3.3 Feeding system solution . . . 47
3.3.4 Validation of the feeding system . . . 52
3.4 Combustion system . . . 54

4 Test, results and discussion **58**
4.1 Critical parameters . . . 58
4.2 Influence of propane secondary flame . . . 59
4.3 Designed burner setup as an analysis tool . . . 60
4.4 Combustion efficiency of the designed burner . . . 62
4.5 Iron flame NO_x emission . . . 64
4.6 Iron flame solid products . . . 65
4.7 Fluidization problem with smaller particle range . . . 67

5 Conclusion **69**
5.1 Present work . . . 69
5.2 Perspectives . . . 71
Annexe . . . 72

A Initial feeder solution **72**
A.1 Description . . . 72
A.2 Tests . . . 73

B Agglomeration problem **76**

C Filter Selection Chart **78**

List of Figures

1.1 Energy consumption forecast for OECD and Non-OECD by region [4]. 2
1.2 Total energy supply [7] . . . 3
1.3 Hourly output of solar and wind energy [8] . . . 4
1.4 Hourly electricity consumption by customer category [9] . . . 4
1.5 Energy density and specific energy of metals candidates compared to hydrocarbons, batteries and hydrogen. [12] . . . 6
1.6 Metal fuel redox cycle [14] . . . 6
1.7 Periodic table for possible energy carrier candidates. [15] . . . 7
1.8 Possible applications of a metal combustion device [12] . . . 9
1.9 Conceptual ship powered by iron [26] . . . 9
1.10 100kW iron combustion system used in a brewery in the Netherlands [28] . . . 10

2.1 Proof of concept of iron used as en energy carrier[30] . . . 12
2.2 Picture of a power generation system using magnesium as fuel [31]. 13
2.3 Experimental setup for creating flat iron flame [32]. . . . 13
2.4 Flat iron flame [32]. . . . 13
2.5 Schematic of the entrained flow reactor used for the combustion of pulverized sponge iron [19]. . . . 14
2.6 Schematic of the particle generator setup [17]. . . . 15
2.7 Particle generator setup [17]. . . . 15
2.8 Schematic of iron micro-gravity combustion experiment inside a rocket [33]. . . . 15
2.9 Representation of the experimental setup used to burn aluminium particles [34]. . . . 16
2.10 Stabilized metal flames compared to methane flame [11]. . . . 17
2.11 Iron powder flame obtained in the master thesis's work at UCLouvain. 18
2.12 Thermal structure of a particle burning in the kinetic and diffusion limit [13]. . . . 19
2.13 Ignition temperature of metals as function of particle size. [13] . . . 21

2.14 T_{ign} as a function of the particle size for different oxide layers. In comparison of a model [43] neglecting the effect of the oxide layer on the oxidation process. [40] 22
2.15 (a) Thermal onset temperature as a function of the equivalence ratio for different suspension radius. (b) Thermal onset temperature as a function of the particle size for different suspension radius and with $\phi_{FeO} = 1$. [40] 22
2.16 Schematic representation of the processes involved in the combustion of particles in suspensions [13] 23
2.17 Heat and mass transport representation within an agglomerate. [13] 23
2.18 Mode of metal particle combustion [11]. 24
2.19 Sketch of the different combustion modes that may occur in a Bunsen-type burner during metal particle combustion [11] 25
2.20 Classification of metals as a function of the ratio between the flame temperature and the boiling point of the metal, and of the partial pressure of the corresponding oxide [11] 25
2.21 Combustion time of a single particle with respect to its radius. [13] 27
2.22 A) Long exposure light streak, B) radiant intensity evolution, C) raw image sequence [17]. 28
2.23 t_{tot} and t_{max} as a function of the particle diameter for different oxygen concentration [17]. 28
2.24 t_{tot} and t_{max} as a function of $1/X_{O2}$ [17]. 28
2.25 a. Burning velocity as function of the particle size and equivalence ratio. b. Comparison of the dependence of the equivalence ratio on the flame speed for metal suspension combustion and methane combustion [12] 30
2.26 Flame speed with respect to fuel concentration in fuel-lean mixture of aluminium-air suspensions obtained by a. Cassel [50] and b. Ballal[51]. Reprinted from [29] 31
2.27 Flame speed as a function of the iron concentration for lean and rich mixture [21] 31
2.28 Burning velocity of aluminium fuel-rich suspension as function of the fuel concentration. a. from experimental results, b. calculated from model [52] 32
2.29 Experimental and theoretical comparison of iron flame as a function of the size [22]. 32
2.30 Iron flame under microgravity [29]. 32
2.31 Gas temperature as function of the equivalence ratio [43]. 33
2.32 Iron particle temperature as a function of the oxygen concentration and particle size [53]. 34

2.33 NO_x emissions from 100kW burner setup [26]. 36
2.34 Influence of the concentration of water added to the combustion on the a) NO_x production and b) O-radicals formed, as a function of the flame front. Note the logarithmic scale for the O-radical graph. [26] 36
2.35 Results of combustion tests comparing 2 types of PSI and coal. Solid residue (SR) and fumes were defined as particles above and below 10μm respectively [19]. 37
2.36 Normalized NOx emission with respect to the equivalence ratio [57]. 38

3.1 Schematic representation of the burner. 40
3.2 Airflow system used in the combustion setup. 43
3.3 Schematic of the force balance on a particle in a moving fluid [36] . 44
3.4 Graphical powder classification as function of particle size and density [36] 45
3.5 Gravity feeder coupled with vibrator suspended at scale [30] 46
3.6 PALAS powder aerosol generator [60] 46
3.7 Venturi Injector [62] 47
3.8 Syringe type feeder used at *McGill University* [63] 47
3.9 Evolution of the first model of feeder. 48
3.10 Feeder model 1 48
3.11 Evolution of the final version of the feeder. 49
3.12 Final feeder cut. Syringe tube in blue, plumber in red. 50
3.13 Final Feeder 50
3.14 Final feeder cut 2. Dark grey is the iron powder 50
3.15 Lead screw slide 51
3.16 Simple experiment to estimate the static friction force inside the syringe tube. 51
3.17 Feeding system 52
3.18 Setup with cold recovery system using first model of feeder 52
3.19 Equivalence ratio as a function of time for different set of parameters. 53
3.20 First iron flame obtained. 55
3.21 Second iteration of the combustion system. 55
3.22 Two pictures of the same flame taken one second apart. 56
3.23 Flame obtained with the fourth iteration of the burner. Pictures B and C taken a few frames apart. 57
3.24 Flame obtained with the fourth iteration of the burner. 57
3.25 Full iron powder setup designed at UCLouvain 57

4.1 Influence of the intensity of the propane flame on the iron flame for the same iron mass flowrate provided for each test. 59

4.2 Largest turbulence of a combustion test for a flame with A) 4kW with $\phi = 1.2$, B) 4kW with $\phi = 0.6$ . . . 61
4.3 Solid deposit forming on the tip of the thermocouple as the iron combustion is occurring . . . 62
4.4 X-ray pattern of combustion products from a combustion with an equivalence ratio of 1 . . . 63
4.5 Mass composition of combustion products for combustion tests at different equivalence ratios. . . . 63
4.6 Thermocouples and exhaust analyser position. . . . 64
4.7 A) Fresh iron powder before combustion, B) Iron oxide powders recovered from combustion. . . . 66
4.8 Oxide particles show cavities formed during the combustion of iron particles. . . . 66
4.9 Obstruction clearance of the feeding system while using 15-53 μm iron particles. Pictures A,B and C are 3 consecutive frames from a video. . . . 67
4.10 SEM images of iron particles from the 15-53μm range . . . 68

A.1 Feeder . . . 73
A.2 Air entrance . . . 73
A.3 O-ring . . . 73
A.4 Schematic representing the different initial position of the powder . 74
A.5 Mass recovery of particle with respect to time with different initial powder position . . . 74
A.6 Influence of air flowrate on iron mass flowrate . . . 75

B.1 A) Fresh iron powder, B) Iron powder after going several times into the cold mode system. . . . 76
B.2 Optic microscope images of A) Fresh iron powder, B) Agglomerated powder. . . . 77

C.1 Particle filter selection guide [66]. . . . 78

List of Tables

3.1 Molar iron mass flowrate for operating limits. 41
3.2 Iron flowrates for operating limits. 41
3.3 Volumetric flowrate of iron and air for operating limits. 42
3.4 Particle group classification 45
3.5 Volumetric flowrate for the two limit cases scenario. 54

4.1 Mass percentage of Fe_2O_3 and Fe_3O_4 measured using XRD analysis from different combustion product samples. 64
4.2 Temperature measured at the three thermocouples for a stoichiometric 4kW flame. 65

Introduction

Nowadays, fossil fuels still supply 80% of the world's energy [1]. Unfortunately, the combustion of carbon-based elements releases GHGs which are known to play a significant role in climate change. Therefore, limiting consumption of fossil fuel is primordial, and turning to renewable energy seems to be the most logical choice, as the sun provides more energy to the Earth in one hour than what humanity consumes over one year [2]. Unfortunately, the power output of such energy sources is intermittent and subject to high fluctuation, and so is the energy demand, which can lead to high excess of energy production. It is then of major importance to find ways to store the surplus of energy and be able to use this energy whenever it is needed.

Metal powders as an energy carrier have been proposed and investigated over last years to achieve this goal. Indeed, metals in powder form are highly reactive and can be burn with air, without emitting GHGs. The solid oxides products can be recovered and later regenerated with some clean excess energy using different reduction processes, to be burned again whenever it is needed and therefore closing a sustainable cycle. Metals shows energy density comparable to those of hydrocarbons, which opens other fields of application compared to alternative energy carrier such as hydrogen and batteries. Metal powders can be useful for building or process heating, used in big transportation or be candidates to retrofit coal power plant.

The content of this thesis can be divided into two parts. First, a state of the art on metal powder combustion is presented. It includes a presentation of different setups that have been developed to observe and study metal powder combustion. The basic principles of heterogeneous combustion are explained. The influence of the input parameters on the combustion properties is addressed.

The second part of this thesis is focused on the design and fabrication of an iron powder burner. The design process and main constituents are presented. The principal difficulties concerning the fluidization and ignition of powders are outlined. The use of the burner for analysis experiments is discussed. The influence of the ignition flame is described and the combustion efficiency of the present setup is obtained. An analysis on gaseous and solid products is conducted. Finally a conclusion will be drawn and perspective for future work will be discussed.

Chapter 1

Context and Motivation

1.1 Energy and climate crisis

Energy is defined by the ability to do some work. Modern civilization was achieved because people learned to convert energy from one form to another and make use of it to do work. Energy is needed to move our cars, to heat our homes or turn on our televisions. It is needed to produce goods and provide services. Energy allows our bodies to grow and our minds to think. The availability of energy has allowed humans to enhance their comfort and quality of life [3]. As population is still growing, energy demand will keep growing as well, with an estimation that the global energy use will increase by nearly 50% by 2050, compared with 2020, coming mainly from non-OECD[1]countries [4], as can shown in Figure 1.1. For

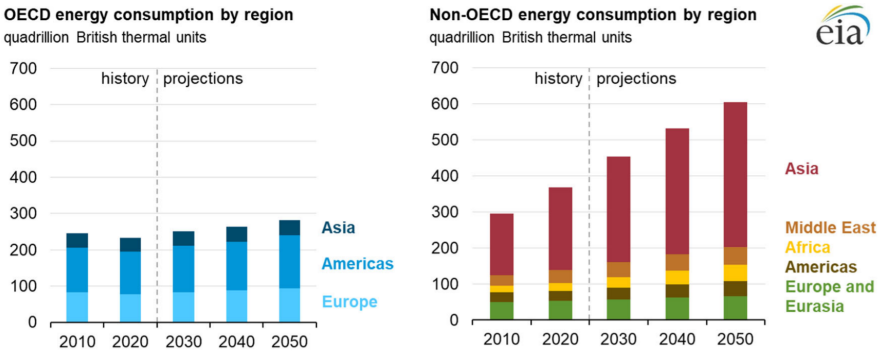

Figure 1.1: Energy consumption forecast for OECD and Non-OECD by region [4].

over 150 years, this energy demand has been fulfilled in great majority with fossil

[1]OECD = Organisation for Economic Co-operation and Development, is an international organisation that works to build better policies for better lives, including mainly developed countries.

fuels. This include coal, oil and natural gas, which represents 80% of the world's energy supply [1]. Regrettably, the combustion of carbon-based elements releases greenhouse gases, including CO_2, which are known to be the main contributor to climate change. In this context, the Paris Agreement aims at limiting the increase of the global average temperature to maximum $2°C$ above pre-industrial levels [5] (1850-1900). To this end, limiting consumption of fossil fuel is primordial in order to achieve net zero carbon emissions by 2050.

A low carbon society will have to rely on a wide range of alternative energy solutions. Biomass as a source to produce biofuels is a potential candidate to help make the transition but many estimate that only a fraction of the energy needs can be replaced by those energy carriers. This is mainly due their low energy density and effectiveness associated with the photosynthesis per footprint of land used [6]. More globally, the potential of renewable energy sources exceeds the world energy demand by hundreds of time. For instance, the solar energy potential is around 3 x 10^6 EJ/year meanwhile the entire world demand is around 16 EJ/year[2]. The sun provides more energy to the Earth in one hour than what humanity consumes over one year.
The International Energy Agency, predicted that, in order to reach net zero emissions by 2050, renewable energy will significantly increase (Figure 1.2), and will supply about 90% of the electricity demand [7].

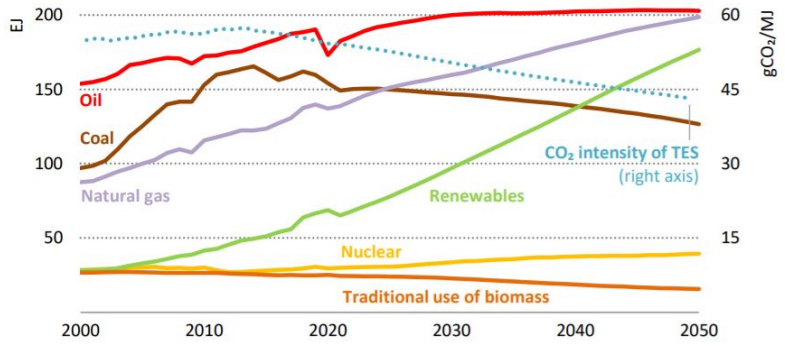

Figure 1.2: Total energy supply [7]

1.2 Power-to-X-to-Power

As the renewable energy is being developped in a promising way for a transition to a low-carbon society, complications emerge. The power output of those kind of energy sources, such as solar or wind, are subject to high fluctuation with respect to time. There can be daily-scale fluctuation, as can be seen in Figure 1.3, to

seasonal timescale fluctuation. In addition of this, the energy demand is also highly inconsistent (Figure 1.4)

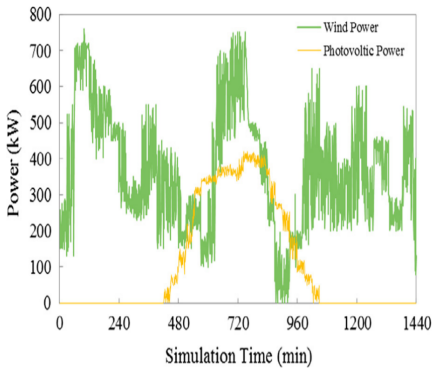

Figure 1.3: Hourly output of solar and wind energy [8]

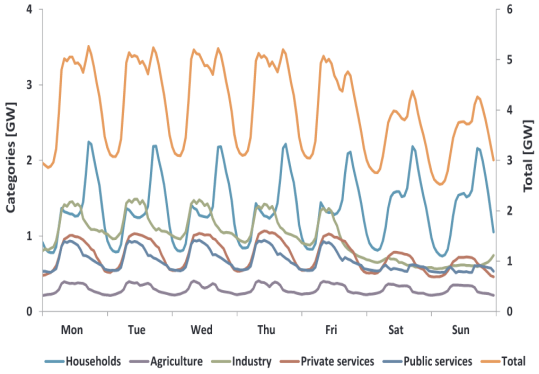

Figure 1.4: Hourly electricity consumption by customer category [9]

When combining these two events, two scenarios may occur. The first one is a power supply shortage for which there is not enough energy output to support the energy demand. This problem of power supply disruption does not exist with fossil fuels, as they can be stored and used whenever needed, whether to compensate primary energy shortage or to meet peak demand. The second scenario is when there is an overproduction of renewable energy. As opposed to coal or gas power plant, renewable energy sources such as solar or wind are intermittent. It is then of major importance to find ways to store the surplus of energy and be able to use this energy whenever it is needed. Power-to-X-to-Power solutions are a key element in a context of energy transition to meet fluctuated energy demand and overcome the unstable nature of the majority of renewable energy sources, and thus be able to synchronize the energy production and energy demand.

Furthermore, fossil fuels play a key role in global trade of energy around the world in view of the fact that some regions are not self-sufficient for their power needs. Those trades concern oil, coal and natural gas which are transported by shipment, trains, trucks or pipelines. Possible candidates for energy storage would need to be traded and transported with similar ways as hydrocarbon fuels.

In the present time, beside large-scale storage systems such as pumped-hydroelectric and compressed air storage that are mainly used for producing electricity connected to the grid, most of the energy storage is done through batteries and hydrogen.

- **Batteries** are good for small devices and short term storage. Unfortunately,

they are subject to very low energy density, meaning that they are not suitable for large-scale energy storage. They can reach high power output but for a short time. Also, batteries can self-discharge, making them useless for long-term energy storage. Batteries are still promising for the car industry with estimations that 31% of the global light-duty vehicle will be composed by electric vehicle by 2050 [4]. But they are not suitable for the energy needs of fields such as industry or big transportation like trains or ships.

- **Hydrogen** is a good energy carrier but current cycle efficiency is relatively low, and also suffers of poor energy density as compressed gas. It can be stored as a cryogenic liquid but the energy density is still one order of magnitude lower than hydrocarbon fuels, and the compression and liquefaction implies severe energy costs [10]. Hydrogen also shows danger during manipulation due to its high reactivity, and requires restrictive safety requirements.

It this then important to find a new way to store and transport energy. A potential candidate would need to be inexpensive, abundant, recyclable using renewable energy, safe, and not a source of greenhouse gases.

1.3 Metal powder as energy carrier

Bergthorson proposed the idea to use metal fuels as clean, recyclable energy carrier [11][12]. Metals have been used for decades to increase the energy content of propellants and explosives. In those application, metal have been used for their high energy density and reactivity due to their high surface-to-volume ratio of the micron-sized fuel particles [13]. Indeed, we can seen in Figure 1.5 that metals possess even higher energy density than hydrocarbons, but usually a lower specific energy. When comparing the same volume of iron and gasoline as an example, iron will contains more energy than gasoline, but will be much heavier. It can also be noted the evident disadvantage of the volumetric energy density for hydrogen and batteries.

The concept of metals as energy carriers is illustrated in Figure 1.6. First, metals, in the form of powder, can be burned with air releasing a similar amount of energy as hydrocarbons fuel. As the metal molecules do not contain any carbon, the combustion of metals do not produce any GHGs. The powder will then oxide and produce only solid products. In a matter of sustainability, it is important to be able to close the cycle. Therefore, those oxide particles can be collected and be reduced back to the initial metal using clean energy such as wind and solar, using for example electrolytic metal-fuel recycling on Figure 1.6. It will be seen

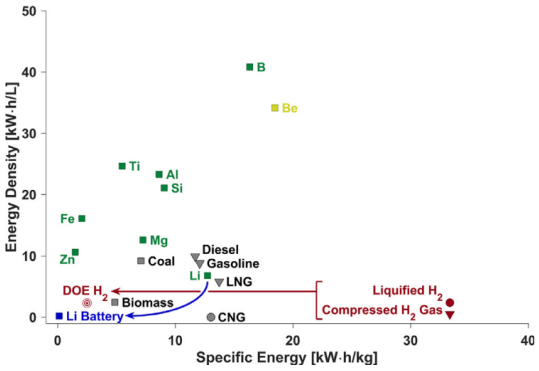

Figure 1.5: Energy density and specific energy of metals candidates compared to hydrocarbons, batteries and hydrogen. [12]

later that other processes exist. Once the initial metal is recovered, it can be burned again. Metal powders as energy carrier are therefore a good example of

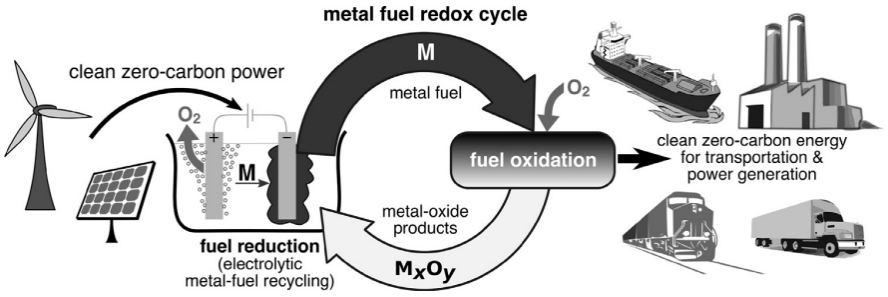

Figure 1.6: Metal fuel redox cycle [14]

the concept of circular economy necessary to achieve sustainable development. If energy production exceeds demand, this excess energy can be stored by reducing the metal oxide into fresh metal powder that can be burned whenever needed.

1.3.1 Metal candidates

When searching for metal candidates to use as energy carrier, the periodic table in Figure 1.7 provides all available options. Firstly, the metal must be able to react if oxygen in order to oxidise, so that elements from groups 15-18 of the periodic table can be set aside. Then, it is desired for the energy carrier to have an high energy density, meaning that periods 5 and higher are eliminated because of their high molecular mass makes their specific energy too low [15]. Hydrogen and carbon are excluded due to their low energy density and the known production of GHGs respectively. Others metals such as scandium, titanium, vanadium, gallium and

germanium have a known reserved that are too low to be considered as an energy carrier on the scale required.

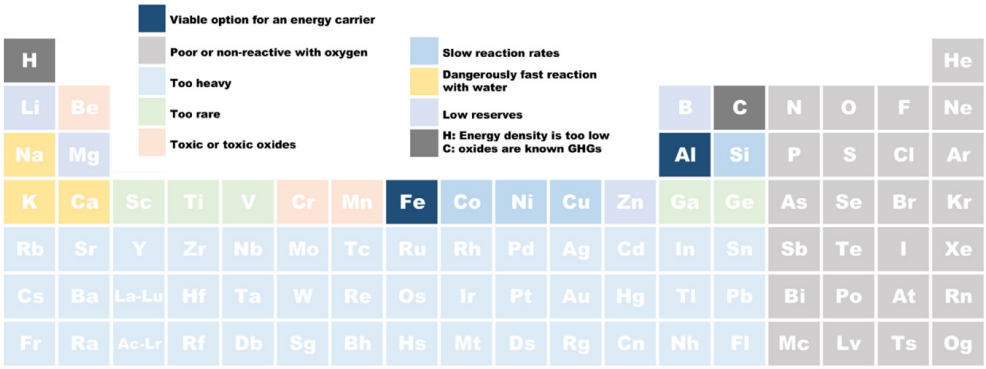

Figure 1.7: Periodic table for possible energy carrier candidates. [15]

When taking into account other criteria such as the reaction rates or toxicity shown in Figure 1.7, only a iron and aluminium are left over. Magnesium could also be a possible candidate, taken into consideration of the sustainable aspect of the cycle, that the initial supply in metal is considered as investment capital. Silicon can also stay in the discussion, even though that only nano-sized particles have demonstrated to have acceptable oxidation rates [16].

Among those four possibles candidates, many believe that iron is the most promising one [12][17][18].

- As will be explained in further section, iron is the only one predicted to form micro-sized metal oxide. Which is an important criteria as nano-sized oxide are much more difficult to recover.
- Iron is cheap and easily accessible.
- Reduction technologies already exists [19][20].
- The flame temperature of iron with air is around 1800-2200K [21][22], which is similar to hydrocarbons. An important parameter when considering the retrofitting of certain facilities using hydrocarbon fuels.

1.3.2 Oxidation and reduction processes

The energy contained in the metal powder needs to be extracted through a process of oxidation. Two distinctive routes have been identify that can exploit the chemical energy of metal powder at high power density [12]. The first one is the wet cycle,

which is through a reaction with water at high temperature that will produce heat and hydrogen, which can itself be used a power generation system. Metals such as aluminium and magnesium are more suitable for this type of oxidation. The second route which will be developed in this thesis is the direct combustion of the metal powders with air

The key element of the whole cycle is the ability of metal oxide to reduce to the initial pure metal. There are several processes available in order to reduce metal oxides. One of the possible processes in order to reduce metal oxide is the direct reduction (DR) process. Another advantage with using iron as a energy carrier is that technology for reducing iron with DR is already commercially available. In most cases, the process is done by using a combination of CO and H_2 as reducing agent. However, technology starts to develop that use only green H_2[20]. This technology could be used in area where there may be high excess of energy. Metals can also be reduced directly using electrolysis reaction or electrowinning, similar to the process used to electrolyze water into hydrogen.

1.3.3 Real life applications of metal powders as energy carrier

Because of the high specific energy and due to the fact that the metal oxides should be collected, it appears more feasible to use metal powders on stationary equipment or large scale transportation applications [12]. The combustion would occur in specialized combustors and would generate a high-temperature nitrogen flux that can be used for heating building, industrial processes or to generate power in the range of applications shown in Figure 1.8. For example, of all hydrocarbons fuels burned in the U.S. industries, 37% is used to generate steam for diverse applications [23]. Such metal powder combustion device could be low-carbon alternative to those applications.

Little research has been done on investigating or creating actual potential applications for metal fuel burners. Wiinika et al. [19] has demonstrated that sponge iron particles has the potential to replace coal in several energy application such as pulverized coal boilers. This can be of crucial importance in reducing global CO_2 emissions, when considering that 46% of global emission produced by fuel combustion comes from coal [24]. Moreover, coal power plants are still getting build today, and have lifespan of more than 40 years [25]. This represents huge investments on which it is important to find alternatives.

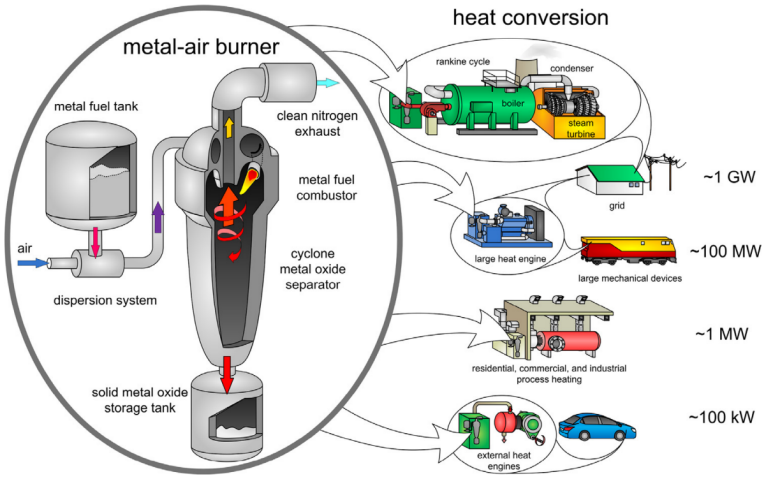

Figure 1.8: Possible applications of a metal combustion device [12]

Members of Eindhoven University of Technology in cooperation with Nederland Maritiem Land studied the technical and economic feasibility of using iron as fuel for ships [26]. It was concluded that the application of iron as a ship fuel is technologically feasible, but that a change of perspective is still needed to make it economically and operationally feasible, and that a fair competition with fossil fuels is an indispensable prerequisite. This technology appears to be most suitable for ships with a high payload/displacement ratio, such as inland vessels and bulk carriers, similar to the one represented in Figure 1.9

Figure 1.9: Conceptual ship powered by iron [26]

Team Solid from Eindhoven University demonstrated a 100kW setup used in a brewery in the Netherlands. This is the first test of industrial application of metal powder as a fuel, with a TRL of 4/5. The system uses the energy contained in the metal to evaporate water and produces steam, which later use it in the brewing

process. The full combustion device is shown in **??**. They are also developing a 1MW combustion system to provide heat to Small and Medium Entreprises (SMEs), in collaboration with the end users [27].

Figure 1.10: 100kW iron combustion system used in a brewery in the Netherlands [28]

Chapter 2

Metal powder combustion state of the art

The combustion of metals have been used for centuries, with their uses as additives to propellant, fireworks, explosives and others. But this is only a few decades ago that began scientific research on the real understanding of the theory behind metal powder combustion. Meaning that the state of science concerning the theory and understanding of metal powder combustion is still in its early stages. This growing interest was motivated by their exceptionally high energy density in order to use them as energetic fuel additive to rocket motors. The combustion of metal particles is a much more complicated problem than gaseous fuel which are mainly hydrocarbons and possesses similar reaction chemistry and thermodynamics. On the other hand, metal combustion is affected by phase transformations such as melting, boiling, sublimation and gasification of the metal itself, but also of the oxidised combustion products.

It is well recognized in the combustion community that difficulties in experimenting heterogeneous flames in the laboratory are the main explanation for why the field of solid fuel combustion is relatively underdeveloped in comparison to the very advanced field of gaseous combustion. [29]. But combustion is an experimental science, and theoretical models need to be validated by experiments.

2.1 Experimental setups

Few studies have been conducted on the realization of setup for burning metal powders. This section is a review of some interesting experimental setups that have been conducted to observe and study the combustion of metal powders, whose results from some of these setups have been used for this master thesis. The

fluidization system aiming to mix metal particles with oxidiser in the following setups will be covered in more details in the section section 3.3.

Prior to the 100kW setup presented in section section 1.3.3, Team Solid from Eindhoven University demonstrated a proof of concept for the use of metal powder as an energy carrier. The iron powder is first mixed with air using a dispersion system. Then the mixture is ignited inside a combustion chamber with the use of an annular hydrocarbon flame. The heat generated by the combustion is later use to produce steam thanks to a sterling engine, finally the oxide product is recovered with a cyclone. The flame power of the flame in this system can reach 20kW. The setup is shown in Figure 2.1.

Figure 2.1: Proof of concept of iron used as en energy carrier[30]

Laraqui et al. [31] also showed a proof of concept by developing a power generation system fueled by magnesium particles. It contains a water-cooled combustion chamber, a cyclone, a secondary heat exchanger, and a particle filter. The magnesium is burned within a swirled-stabilized flame in order to provide good mixing and to enhance flame stability at lean condition. Four tangential inlets were used to create the swirl. The magnesium/air mixture is ignited using a pilot hydrocarbon flame, which is then turned off when the flame is stabilized. The setup is shown in Figure 2.2.

McRae et al. [32] introduced a setup capable of producing a flat flame. This type of flame allows for better study of fundamental combustion properties, such as flame speed, due to a simplified 1-dimension flame which allows a better geometry for the measurement experiments. The setup is shown in Figure 2.3. A mixture of

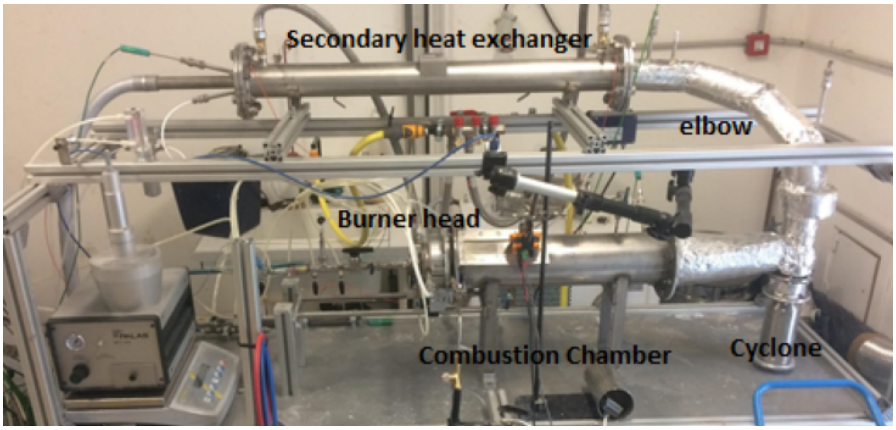

Figure 2.2: Picture of a power generation system using magnesium as fuel [31].

iron and air/argon is exiting a bottom nozzle. A second nozzle which is inverted produces a stoichiometric methane flame that is concentric to the bottom nozzle. The two flows meet at a stagnation point where the exhaust gases from the methane flame are sufficiently hot to ignite the iron particles without other sources of heat. Optical means were used to measure the flame speed of the burning iron particles.

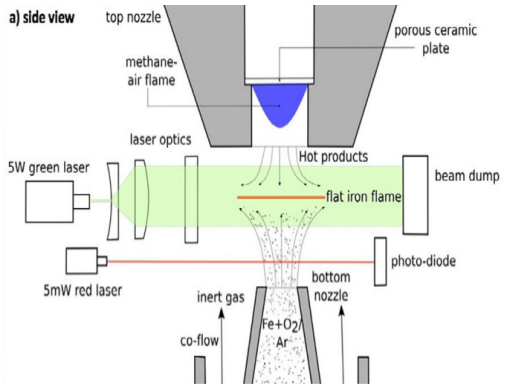

Figure 2.3: Experimental setup for creating flat iron flame [32].

Figure 2.4: Flat iron flame [32].

Wiinika et al. studied the combustion of Pulverized Sponge Iron and the resulting gaseous and solid products. They have used a small-scale Entrained Flow Reactor (EFR), which have been commonly used to study pulverized coal combustion. The EFR consists of a 2m vertical tube with a diameter of 5cm, which is installed in an electrically heated tube furnace. The temperature of the tube furnace is $1400°C$, which is enough to ignite the iron particle without any additional heat sources. The solid combustion products were than separated from

fumes using a cyclones. The fumes were analysed. A representation of the setup is shown in Figure 2.5.

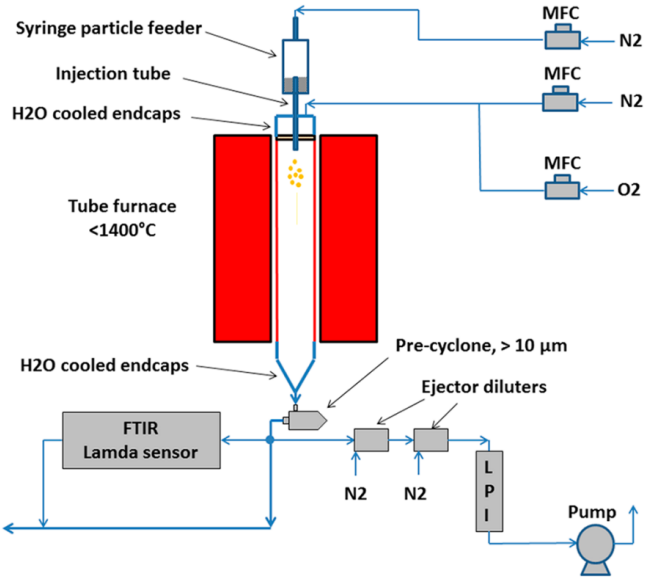

Figure 2.5: Schematic of the entrained flow reactor used for the combustion of pulverized sponge iron [19].

Ning et al. [17] focused on iron single particles combustion. They build a setup using a particle generator based on electrodynamics powder fluidization. This setup is able to "generate a single metal particle moving upward with a well controlled velocity and trajectory, and ignite it at near-uniform conditions by an infrared laser beam with flattened elliptical beam profile" [17]. A schematic is shown in Figure 2.6. First, the particles are fluidized with a single particle generator represented in Figure 2.7. The powder is aerosolized by applying a DC voltage between two horizontal electrodes inside an enclosed chamber until a steady cloud is formed. Then the gas mixture coming from a central jet exits through the top electrode in an extremely thin tube, while dragging some particle with it. Once the particle is ejected of the generator, it is ignited using a 75W laser.

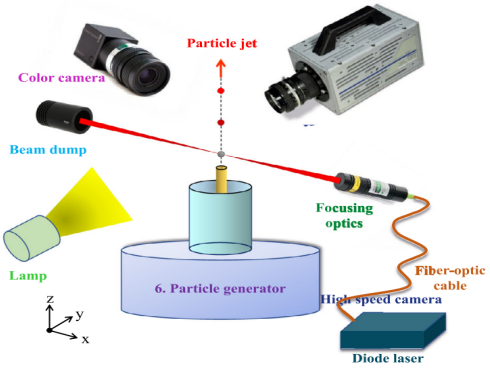

Figure 2.6: Schematic of the particle generator setup [17].

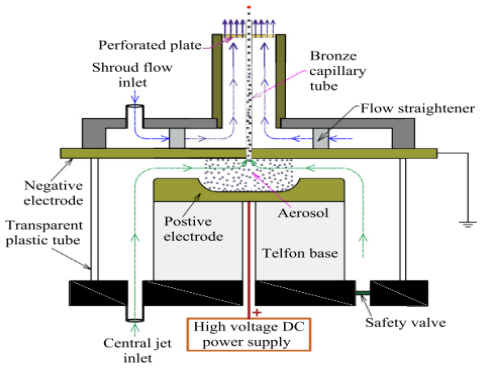

Figure 2.7: Particle generator setup [17].

Palecka et al. [33] measured the combustion of powder clouds in micro-gravity environment. Using this technique, effects such as particle sedimentation, bulk instabilities or buoyancy-induced convective flows are decreased and permit a better observation and understanding of the combustion properties. In order to perform these experiments, tubes in which the combustion will occur were placed on a MAXUS-9 rocket lunched by the European Space Agency. The tube was then filled with an iron suspension and was ignited using an electrical spark on one hand of the tube which was open. A representation of the experiment is shown in Figure 2.8.

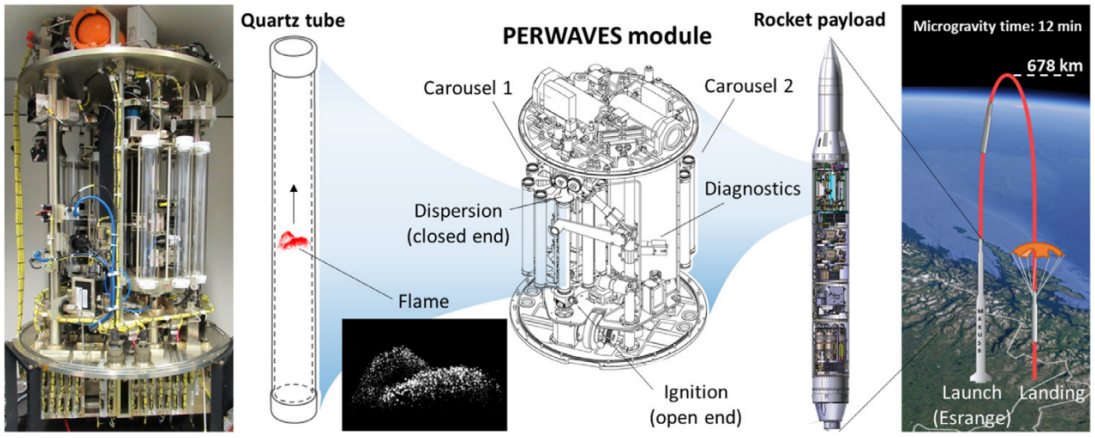

Figure 2.8: Schematic of iron micro-gravity combustion experiment inside a rocket [33].

Lomba et al. [34] realized a Bunsen-type burner to examine the combustion of

aluminium particles. A mixture of air and methane is mixed with aluminium particles. It is then ignited at the nozzle using an annular pilot flame, creating an hybrid Al/CH_4 flame. Once the flame is stable, the methane supply is closed and the aluminium flame stabilized by itself. The flame is then characterized using a camera, a tomography setup, a spectrometer and filter. The setup is shown in Figure 2.9

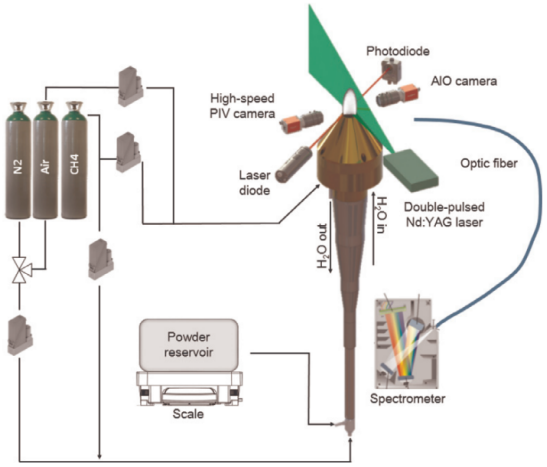

Figure 2.9: Representation of the experimental setup used to burn aluminium particles [34].

2.2 Metal powder combustion theory

In order to develop robust metal fuel burner, it is necessary to well understand the different combustion mechanisms of metal powders. Knowing under which circumstances a particle or suspension will ignite is crucial, as well as knowing the influence on an input parameter such as the particles size on the different combustion properties, for example the burning velocity. This section aims to grasp the fundamentals of metal powder combustion and to gather the different studies that have been performed on the subject. During the combustion, solid particles will interact with a gaseous oxidiser, creating an heterogeneous flame.

2.2.1 Heterogeneous flame

Homogeneous combustion have been widely studied over the years and possesses now a qualitative theoretical background. Unfortunately this is not the case for heterogeneous combustion. But first it is important to well distinguish the two.

Homogeneous combustion is often defined as the ones with a visible gaseous flame, as heterogeneous combustion is defined as combustion in which a solid or liquid and a gas react together to oxidise. However, heterogeneous flames can also have an identical appearance as gaseous flames as can be seen in Figure 2.10. Also, other

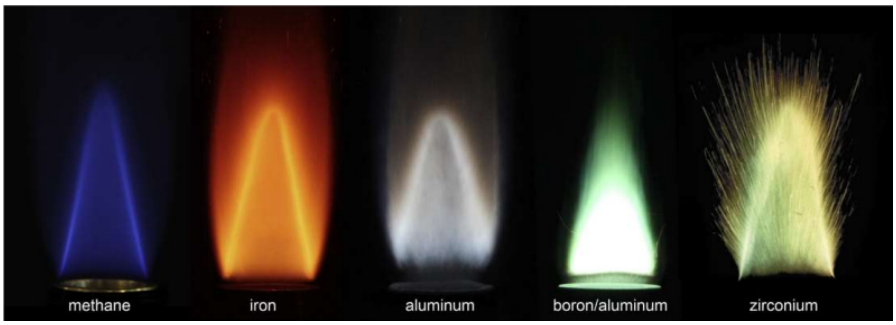

Figure 2.10: Stabilized metal flames compared to methane flame [11].

solid materials such as plastics burn in a homogeneous manner due to the fact the plastic will melt and volatilize readily in the preheat zone, and is than comparable to hydrocarbon sprays. It is then important to establish the limit between the two regimes of combustion. The key parameter to define a homogeneous combustion will be the ability of the fuel to volatilize and form a gaseous/oxidiser mixture before combustion. There are some complex fuel such as coal that can burned in a mixed mode. Indeed, coal possesses a lot of components that can volatilize and burn in a gaseous flame, while the solid residue, the char, burns in a heterogeneous regime of combustion. [35]. This criteria is necessary but not sufficient to ensure that a fuel will burn homogeneously. Another parameter is the stability of the gaseous-oxidiser mixture at temperature close to the boiling point of the metal. At those temperature, the reaction between metal vapor and oxygen is almost instantaneous and it is anticipated that the newly formed metal vapor will not be able to mixed with the oxidiser before burning, and thus cannot form a homogeneous mixture. This is why most metals tend to react heterogeneously. It will be covered in more detail in the next sections which metals burn heterogeneously and in which conditions. [29].

2.2.2 Fundamentals on metal powder combustion

This section aims to understand the basic principles of heterogeneous combustion, and more specifically the combustion of metal powders. Aspect such as the combustion regime and the ignition characteristics are key elements in combustion theory. As well as the influence of the different changes of state of metals and their oxides during combustion.

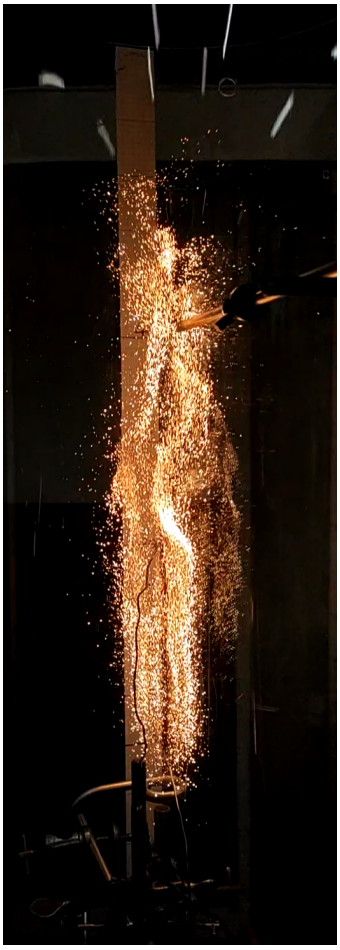

Figure 2.11: Iron powder flame obtained in the master thesis's work at UCLouvain.

2.2.2.1 Combustion regime and ignition

Combustion of solid particles is basically a two-step process. First, the transport of the oxygen to the surface, and secondly, the reaction with oxygen. Tow regimes of combustion can be distinguished and governed by the rate of the chemical reaction (kinetic rate) and transport of the oxygen (diffusion rate). The first one occurs when the rate of the reaction is much slower than the rate at which the oxygen reaches at the surface of the particle. The overall process of combustion is then **kinetically-controlled**. In the second regime, the mass-transfer rate is much slower than the reaction rate, so that the oxygen arriving at the surface of the particle is instantly consumed by the combustion. This is the **diffusion-controlled** regime. We can also identify a intermediate regime when both rate are comparable[36].

It is now of primary importance to identify under which circumstances a metal particles will burn in a given regime. Kinetically-controlled combustion of metal is known to be very comparable to homogeneous combustion, with the rate of the reaction being exponentially dependent on the environment temperature, and scaling linearly with oxygen concentration. This regime especially occurs during the preheating of a particle. Moreover, if the kinetic rate of the reaction is sufficiently fast, the particle can ignite and enter the diffusion-limited regime, in a process called thermal runaway. The main particularity of heterogeneous flames is that, once ignited, metal particles react in individual diffusion-limited regime, forming micro-diffusion reactors that can efficiently burn even in relatively cold surrounding gases. This will lead to their unique appearance of **flames within the flame** combustion front structure, as can be seen in Figure 2.11.

As the particles are burning in autonomous micro flames, it is important to well distinguish the particle temperature to the gas temperature. In the ideal case, when a particle, burn in a kinematic regime, it will burn at the temperature of the bulk gas [13]. On the other side, a particle burning at the diffusion limit will burn at the stoichiometric adiabatic flame temperature, while the bulk gas stays at a relatively cool temperature, as can be seen in Figure 2.12. In practice, a particle will burn in a intermediate regime as the diffusion and kinetic limits are never completely reached.

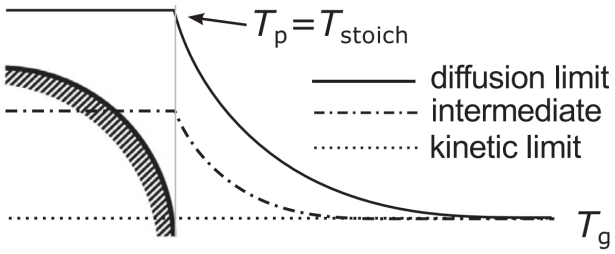

Figure 2.12: Thermal structure of a particle burning in the kinetic and diffusion limit [13].

Soo et al. [13] used a simple thermodynamics approach to analyse the ignition and combustion regime of singles particles, agglomeration and particles in suspensions. The model considers "ideal, non-volatile fuel particles undergoing heterogeneous reaction controlled by a combination of diffusion and kinetic rates" [13], and was establish by Frank-Kamenetskii [37] and further developed by Vulis [38]. This minimalistic model does not take into account the different complications resulting from the different phase transitions and gas-phase reactions. Also, during the combustion, the particle get smaller while the oxide product vanishes, which

is more representative of a metal burning in a vapor phase such as aluminium, as it will be explained in more details in the next section. Indeed, the numerical value chosen for the graphical representation of this model, that would be present several time in this master thesis, are those for an aluminum particle burning in air. Using this model, they have shown that even though large particles is controlled by a diffusion regime, reaction of smaller particles may be controlled by a kinetic regime. Before looking into the ignition of particles in suspension, it is crucial to well understand the combustion of isolated metal particles.

When looking at the thermal balance of a system during the oxidation of metal particles, two processes oppose each other. The first one is the rate of heat release during the reaction, given by:

$$\dot{Q}_R = q\upsilon A_p \dot{\omega} \tag{2.1}$$

Where q is the heat of the reaction per unit mass of the solid, υ is the stoichiometric coefficient relating the mass of solid fuel consumed per mass of oxidizer in the reaction, $A_p = 4\pi r_p^2$ is the particle surface area, and $\dot{\omega}$ is the rate of oxidizer consumption.

As opposed to the heat loss from the particles to the surrounding. It is assumed for simplicity that the molecular conductive heat transfer is the main mechanism of heat loss from the particle. The rate of heat loss is thus :

$$\dot{Q}_L = h_p A_p (T_p - T_g) \tag{2.2}$$

With h_p the heat transfer coefficient, T_g the gas temperature and T_p the particle temperature. Ignition will occur when the rate of the reaction is sufficiently fast, so that the rate of heat release from the heterogeneous surface reaction surpasses the heat loss to the surrounding, in a process called thermal runaway. The ignition temperature can be obtain by the Semenov criteria [39], which states that :

$$\dot{Q}_R = \dot{Q}_L \text{ and } d\dot{Q}_R/dT_p = d\dot{Q}_L/dT_p \tag{2.3}$$

After some calculations that are outside the scope of this thesis, the resulting trend for the ignition temperature obtained by Soo [13] is represented in Figure 2.13.

As the initial size of the particle is getting smaller, the heat release rate of the reaction ($\propto \ d_{p,0}^2$) decreases much more rapidly than the heat loss from the particle ($\propto \ d_{p,0}$) [13][40]. It it then necessary to have a higher reaction temperature to compensate the heat loss from the particles. Therefore, the ignition temperature will increase with decreasing particle size. It can be seen on Figure 2.13 that there is a critical particle size at which the particle cannot ignite and stays in the kinetic regime. For particle that are larger than the critical size but close to it, they may

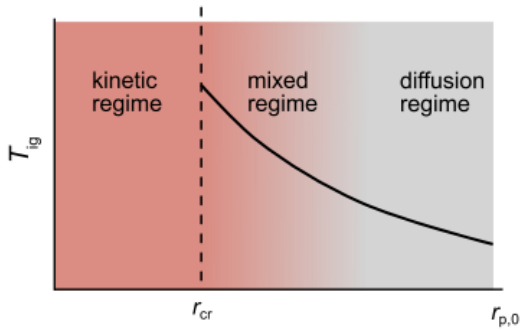

Figure 2.13: Ignition temperature of metals as function of particle size. [13]

ignite in the diffusion regime than later quench after burning down to some size and transition back to the kinetic regime. While particles much larger than the critical limit can burn mainly in the diffusion regime as *micro-diffusion reactors* that are isolated from the surrounding gas.

XiaCheng et al. [40] studied the ignition characteristics of fine iron particles (1μm to 100μm) while also considering an initial oxide layer. Using two different models, they have demonstrated that the ignition temperature of single isolated particle, T_{ign}, depends on the initial oxide layer thickness,δ_0, regardless of the absolute size of the particles. And that for $\delta_0 \leq 0,003$, the ignition temperature is independent of δ_0, as shown in . The corresponding ignition temperature under standard condition is approximately 1080K for any particle size greater than 5μm. Experimental results [41, 42] for the ignition temperature in the range of 1200K are slightly higher than the prediction made by XiaCheng, but significantly higher than what a model that does not take into account an initial oxide layer can predict, as seen in Figure 2.14.

This approach is in contrast of the results obtained by Soo et al. [13], as they did not take into account the effect of the oxide layer for the case of iron particles, but they may still be correct concerning the critical size for ignition of metal particles that do not produce a oxide layer shell around their pure metal core.

When metal particles are in suspension, the reaction rate can be accelerated through the collective effect. Indeed, the heat release of the reaction is transferred to the surrounding gas. As the gas temperature increases, the exothermic reaction rate will increase as well, leading to a *reaction onset* of fuel suspension, at temperature lower than for isolated particles. In theory, any temperature can trigger a reaction onset in a adiabatic suspension, even though the delay time at low temperature are unrealistically long. In practice, heat losses to the surrounding allows that the thermal onset is possible only above a certain heat-release rate, corresponding to a

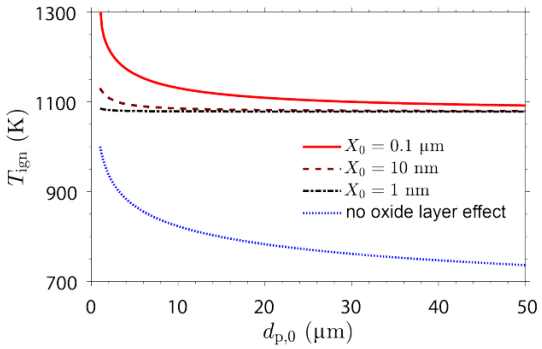

Figure 2.14: T_{ign} as a function of the particle size for different oxide layers. In comparison of a model [43] neglecting the effect of the oxide layer on the oxidation process. [40]

critical external temperature. Above this temperature, the suspension can self-heat until reaching the thermal runaway. The effect is even more pronounced as the suspension radius is getting larger, as can be seen in Figure 2.15(a).

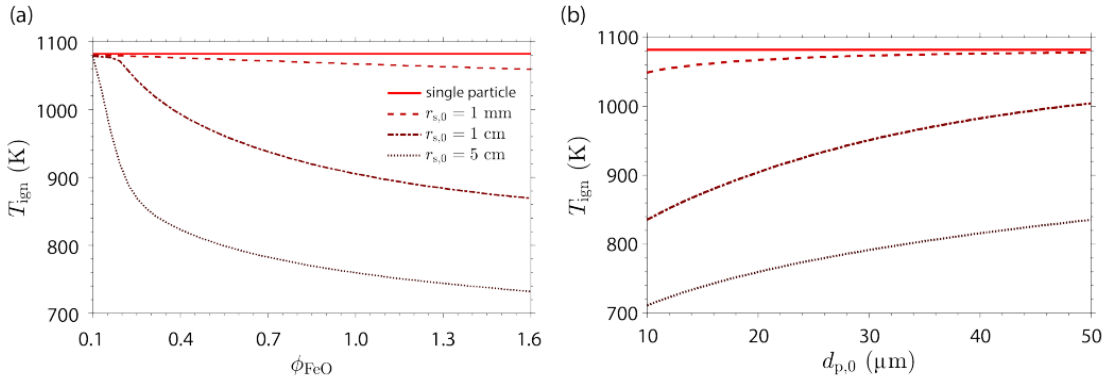

Figure 2.15: (a) Thermal onset temperature as a function of the equivalence ratio for different suspension radius. (b) Thermal onset temperature as a function of the particle size for different suspension radius and with $\phi_{FeO} = 1$. [40]

For a fixed metal concentration, the temperature for thermal onset decreases with decreasing particle size, as shown in Figure 2.15 (b). This is explained by the fact that in a given suspension size, the internal effective area for exothermic reaction will be larger for smaller particle size, while the heat loss from the suspension to the surroundings will be the same. This reaction onset can be independent to the particle ignition end be referred as cloud ignition. It means that even though individual small particles may not ignite and transfer to the diffusion limited regime, they can still efficiently burn in a kinetic regime under a dense fuel suspension.

This process is analog to the reaction onset of homogeneous gas mixture. This suggests that the

Particles in suspension often agglomerate before combustion, which will influence greatly the combustion behavior compared to a single particle, the situation being represented in Figure 2.16. Indeed, while the oxidizer diffuses from the external

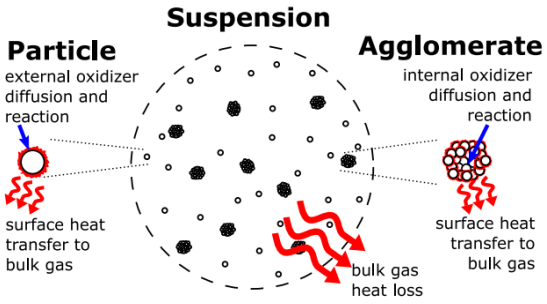

Figure 2.16: Schematic representation of the processes involved in the combustion of particles in suspensions [13]

surface of the agglomerate into the the pores inside of it, a large area undergoes an exothermic reaction. In contrast, only the external surface of the agglomerate contribute to the heat loss to the surroundings, as represented in Figure 2.17.

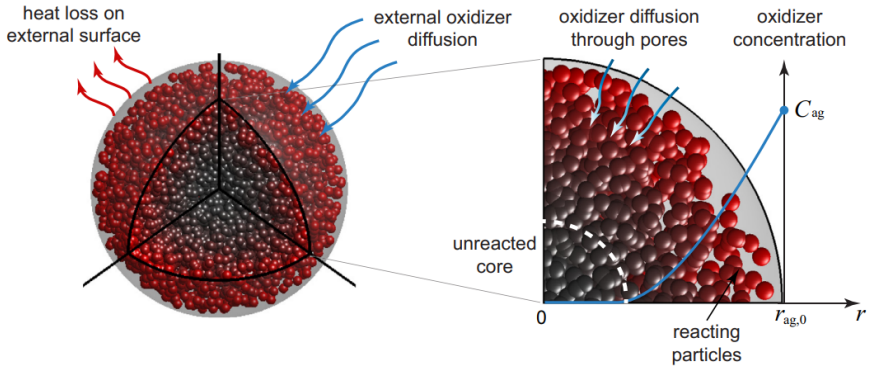

Figure 2.17: Heat and mass transport representation within an agglomerate. [13]

But it is difficult to know if agglomerations are present or not, as it often a hidden parameter, and that their presence can be easily misinterpreted as a specific property of the fuel or to the combustion device. [13]

The increasing temperature in a system is a function of the balance on the heat release from the reaction and the heat loss to the surrounding of the system.

Therefore, the ignition temperature of a same metal can be very different according to the dispersed system (single particle, particle suspensions or agglomerate). The difference can span through several hundred, or even thousand degrees. For example, a single boron particle ignites in air at about 1800-1900K, a dense suspension ignite below 1500K, while boron agglomeration can ignite as low as 750K [13].

2.2.2.2 Diffusion-limited combustion modes

As mentioned in the previous section, once the ignition has occurred in a kinetically-controlled regime, the metal particles can transfer to the diffusion-controlled regime where it will burn as individual micro-reactors. In that combustion regime, metal particles can burn in several different modes of combustion. As stated before, particles burning in a diffusion controlled regime will burn at a temperature close to the adiabatic flame temperature of stoichiometric mixture. At these temperatures, most metals boil, and even evaporation can occur. This is the case for metal particles, but also for the metal oxide products of combustion. Glassman [44] pointed out that the flame temperature of metals is **limited** to the evaporation temperature of the metal oxide combustion product, since the oxide volatilization process would absorb any additional heat release and prevent the flame temperature from increasing.

We can know identify two cases scenarios: if the flame temperature is lower than than the boiling point of the pure metal, the metal particles will not evaporate during the combustion and will thus burn heterogeneously, as illustrated in Figure 2.18B and C.

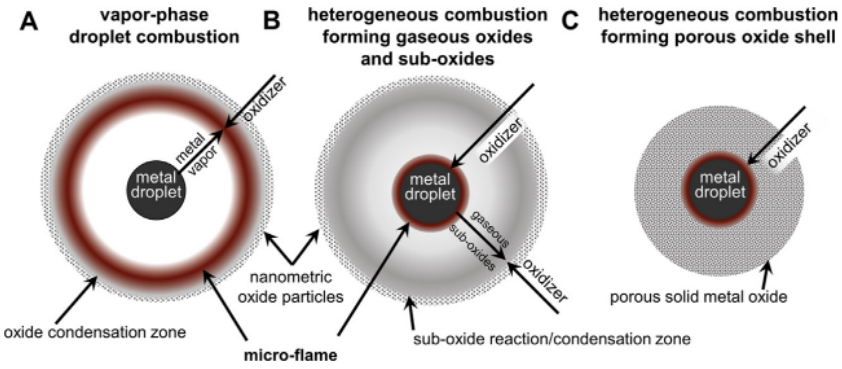

Figure 2.18: Mode of metal particle combustion [11].

The distinction between the two is that is that in combustion mode B, the flame temperature is above the melting point of the oxide. Therefore, gaseous

metal oxide is formed and can thus diffuse away from the particle surface, which will later form nano-oxide particles during the condensation. In combustion mode C, the oxide product is formed directly on the surface on the metal droplet surface, therefore forming a micro-sized oxide product, as can also be seen in Figure 2.19.

If the flame temperature is above the boiling temperature of the metal, it will burn in a vapor phase, as a micro-diffusion flame that is formed around the core of the particle that is not yet evaporated, as can be seen in Figure 2.18A. In order to know if a metal will burn in mode B or C, Bergthorson [11] specified a criteria on the partial pressure of the oxide, stating that if the partial pressure of the oxide is below 10^{-4}, the metal is expected to burn in combustion mode C. As can be seen in Figure 2.20, only iron is predicted to burn in combustion mode C.

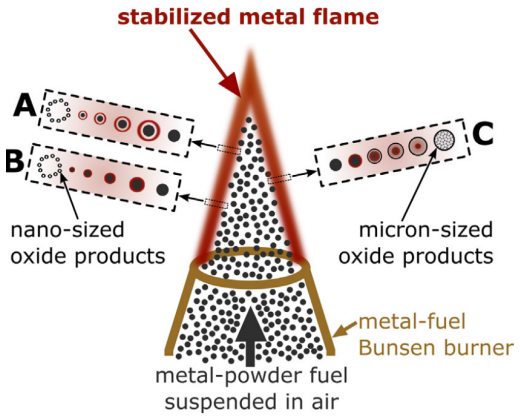

Figure 2.19: Sketch of the different combustion modes that may occur in a Bunsen-type burner during metal particle combustion [11]

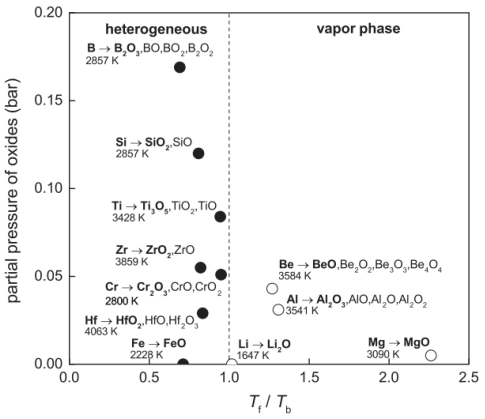

Figure 2.20: Classification of metals as a function of the ratio between the flame temperature and the boiling point of the metal, and of the partial pressure of the corresponding oxide [11]

Having an efficient recovery of the metal oxide particles is a key element in the process, so that a maximum amount of oxide can be reduced in order to have a sustainable cycle. In that context, it is much preferable to use metal that can burn in combustion mode C, as nano-particles are difficult to recover. The graph shows that aluminium and magnesium, which are two serious candidates in the use of metal powder as energy carriers, are expected to combust in a vapor phase, which will lead to complication when trying to capture their oxides.

It is important to note that the combustion modes discussed above, depend also

on the experimental condition of the combustion, and that different set of parameters may results in different products for the same initial metal fuel temperature. For example, Wiinika et al. [19] studied the combustion of Pulverized Sponge Iron (PSI). They found out that a small part of the iron (around 4%), vaporized during the combustion and latter formed nano-size oxide through condensation. Palecka [33] and Toth [18] also encountered some vapor phase combustion of iron droplets. Also, Laraqui et al. [31] performed combustion of magnesium particles in the range of 50-to-70μm, inside a confined combustion chamber. Laser granulometry on the metal oxide product showed a particle mean diameter of 500nm, which validates the theory of vapor phase combustion of aluminum. Nevertheless, more than 98% of the particles were trapped inside the system, thanks to the the tendency of the nano-particles to form micro-sized agglomerate.

2.2.3 Influence of input parameters on metal combustion properties

When talking about combustion of metal powder, it is important to determine the main input parameters and combustion properties. Doing so, one can identify the key factors of metal powder combustion and which inlet parameters have the most influence on a given property. The main output properties that have received particular attention in the past decades and that will be studied in this master thesis are the burning velocity, burn time and emissions.

It must be emphasized that it is difficult to compare results from different studies because combustion often occurs in widely different conditions. Indeed, each powder manufacturers may have an unique set of size distribution, shape, purity, that can interfere the results of experiments. This is not the case for gaseous hydrocarbons which possess the same physico-properties around the world. The main focus may not be on the absolute result itself but on the evolution of combustion characteristics when tuning a specific parameter. The first combustion property that will be looked into is the burn time.

2.2.3.1 Burn time

Combustion time reflects how rapidly the energy of a particle is released. The theory on the combustion of solid particles done by Glassman [44] points out that a particle burning in a diffusion-controlled regime possesses a burn time that has a d^2 relationship with respect to the initial diameter of the particle, a $d^2 - law$. On the other hand, kinetically-controlled combustion is described by a $d^1 - law$. Therefore, a general power law of $t =\propto d^n$ is generally used in order to characterize

the combustion time of metal particles. Once again, a particular caution must be taken into account while trying to compare different studies, as even the definition of burn time may differ. For example, Ning [17] defined the burn time as the total light emission, from ignition to quenching. While Soo et al. [13] defined the combustion time as "the point in time where the particle size is reduced to 1% of its initial radius".

Sun et al. [45] measured the burn time of 1 to 7 μm iron particles in propagating dust flames, and found that the burn time is proportional to particle diameter - thus following a $d^1 - law$ - when it is smaller than about 4 μm. But when particles get bigger, the law demonstrates an higher order of magnitude on the particle diameter dependency, with then n>1. Based on their results, it can be concluded that iron particles burn in a kinetically-controlled regime under a critical diameter value. This was later showed by Soo et al. [13] in Figure 2.21 with the model described in section 2.2.2.1, where the two distinct trends can be observed.

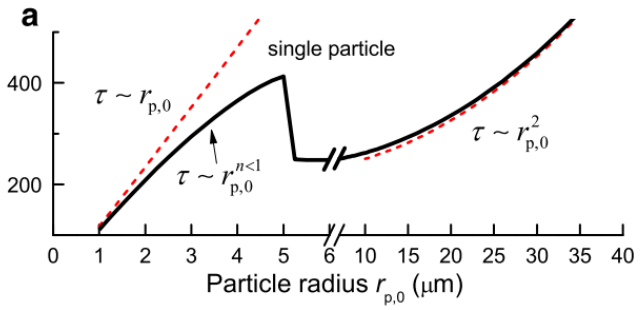

Figure 2.21: Combustion time of a single particle with respect to its radius. [13]

The slight deviation from the $d^1 - law$ for small particles is explained by the slight overheating of the particle temperature above the gas temperature, due to the inability of a small particle to ignite, but also start to be affected by the diffusion limited regime. Also, particles burning in a mixed regime can ignite in a diffusion limited regime, but are susceptible to be extinguished at a non-negligible mass. So that the rate of reaction is dependant not only on the diffusion regime but also on the temperature-dependant kinetic regime after extinction, so that it does not follow either trend.

Ning et al. [17] used the setup described in section 2.1 to measure the combustion time of single ignited particles. The particles used during the test were spherical iron particles with range of 26-54 μm. Also, the particles were burned in an O_2/N_2 mixture with an oxygen concentration varying from 21% to 36%. Thanks to the right type of equipment, they managed to measure the intensity of the burning

particles. Two characteristic times were related to the combustion: 1) total duration of the high temperature phase, t_{tot} and 2) the time to reach maximum brightness, t_{max}, that can be related to the maximum temperature of the particle, as shown in Figure 2.22.

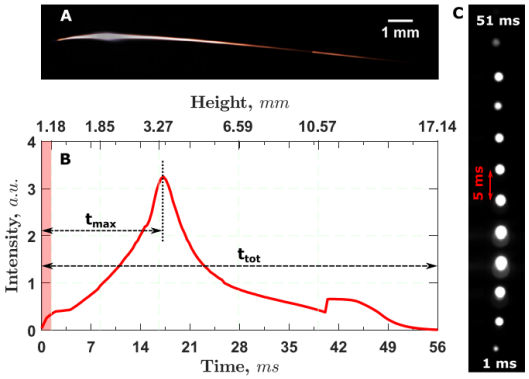

Figure 2.22: A) Long exposure light streak, B) radiant intensity evolution, C) raw image sequence [17].

Results from their experiments can be seen in Figure 2.23. They have shown that the total duration of light emission and the duration to reach maximum brightness are given by the law:

- $t_{tot} = 0.063d^1.72$ and $t_{tot} = 0.097d^1.57$ for $X_{O_2} = 0{,}21$ and $0{,}36$ respectively
- $t_{max} = 0.040d^1.60$ and $t_{tot} = 0.040d^1.60$ for $X_{O_2} = 0{,}21$ and $0{,}36$ respectively

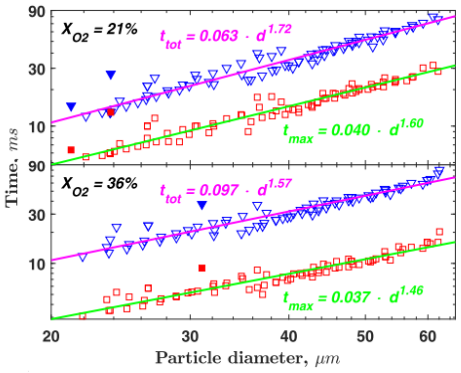

Figure 2.23: t_{tot} and t_{max} as a function of the particle diameter for different oxygen concentration [17].

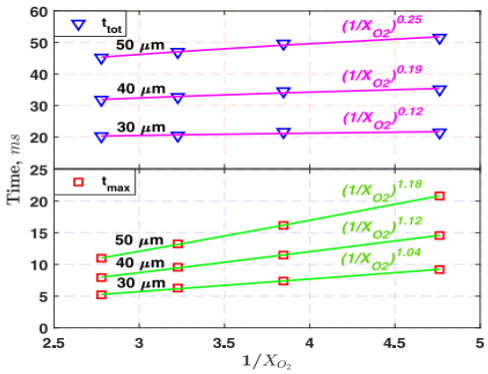

Figure 2.24: t_{tot} and t_{max} as a function of $1/X_{O2}$ [17].

The Glassman theory point out that a particle burning in a diffusion-limited regime would have a $d^2 - law$ relationship with the initial particle diameter, while the kinetically-controlled regime would use a $d^1 - law$ [44]. Unfortunately, the $d^2 - law$ for the diffusion-limited regime have never been experimentally confirmed yet. A possible explanation is that Glassman did not consider internal oxygen diffusivity inside the particle when trying to reach the core of pure iron through the pores. Factor that can greatly influence the behavior of the combustion. For example, Nelson et al. [46] has shown that the internal diffusion of oxygen in the process of combustion of zirconium was a limiting factor. The results in this experiment suggest that the actual regime of the overall combustion process would be situated in an intermediate regime between the two.

In Figure 2.24, it can be seen that the total burn time has a small dependency on the oxygen concentration, while the burn time to reach maximum brightness has a linear relationship with $1/X_{O_2}$. But it is important to note that t_{tot} includes the information of t_{max}, so that the small dependency of the total burn time on the oxygen concentration may be due mainly to t_{max}. Ning hypothesized that the combustion process of single iron particle can be distinguished into two different steps, each with their own sensitivity to the oxygen concentration. Indeed, the linear relationship of t_{max} with $1/X_{O_2}$ indicates that the combustion occurs in an **externally diffusion controlled regime**, because this is the expected relationship when "the same amount of oxygen is consumed by a particle for the same particle size at different oxygen concentrations" [17]. On the other hand $t_{dec} = t_{tot} - t_{max}$ shows very little influence to the oxygen concentration, which suggests an **internally diffusion controlled** regime.

It must be emphasized that those results concern the burn time of single iron particles and may differs from combustion of other metals or in flames.

Key points of this section :

- General power law for burn time : $t \propto d^n$, with n = 1 for kinetically-controlled and n = 2 for diffusion-controlled
- Total burn time of single iron particles $t_tot = 0.0063d^1.72$ which indicates an intermediate regime
- Single iron particle combustion has a low burn time dependency on the oxygen concentration
- Single iron particle combustion occurs in an externally diffusion controlled regime until reaching maximum brightness, then transfer to an internally diffusion controlled regime

2.2.3.2 Flame speed and Burning Velocity

One fundamental property of metal combustion and fuels in general, is the burning velocity. It reflects the intensity of combustion, so that a more reactive fuel will burn with a faster burning velocity [11]. The burning velocity is defined as the speed at which a laminar, planar, one-dimensional, unstretched flame front propagates relative to the unburned gases in front of it [47]. Although real flames rarely satisfy the criteria cited above, experimental results show that the burning velocity can be extracted from the flame speed [29][48]. This is an essential concept when analysing performances of engines and designing combustion devices. Indeed, higher flame speed would result in a more compact and higher power density system [11].

The overall influence of the equivalence ratio and particle size on the burning velocity has been predicted by Soo et al. [49] using the model introduced in section 2.2.2.1. Results are shown in Figure 2.25a. Concerning the size of the particles, above a certain minimum equivalence ratio (around $\phi = 0,45$ regarding this model), the overall trend is that the burning velocity decreases when increasing particle size. This is explained by an increase of the specific area [49]. Particles burning within the diffusion regime are expected to burn with a $u_b \propto 1/r$ relationship, while the ones burning in a kinetic regime are expected to have a $u_b \propto \sqrt{1/r}$ dependence of the particle size on the burning velocity. As can be seen in Figure 2.25, For near stoichiometric mixture, the $\phi = 1$ curve in Figure 2.25a shows a smooth transition between the two regimes.

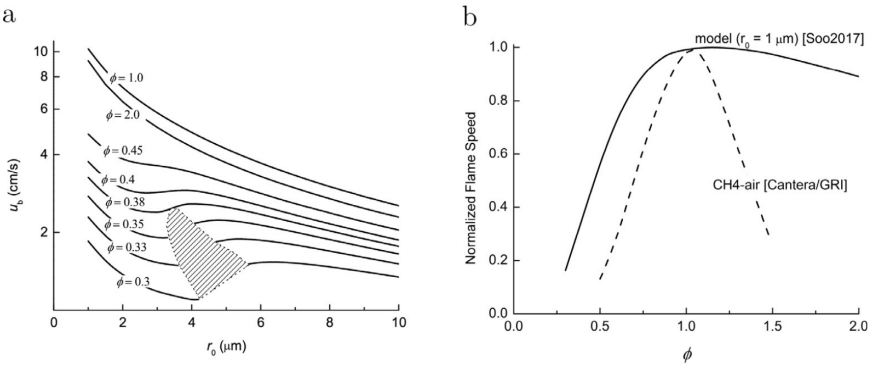

Figure 2.25: a. Burning velocity as function of the particle size and equivalence ratio. b. Comparison of the dependence of the equivalence ratio on the flame speed for metal suspension combustion and methane combustion [12]

Figure 2.25b. shows the comparison of the burning velocity between solid particles and methane when tuning the equivalence ratio. It can be seen that the behavior is similar to that of homogeneous mixture in lean concentration. This is

very different for **fuel-rich** mixture. In that case, the burning velocity decay much more slowly when increasing the fuel concentration. The explanation is simply that, since the fuel is a solid, it occupies practically no volume compared to a gaseous fuel. In other words, adding more fuel will not displace the oxidizer and thus the amount of fuel burned remains constant even with concentration above the stoichiometric equivalence.

Comparison must now be done on experimental work in order to validate this model. Experimental measurement on the flame speed of **fuel-lean** aluminum mixture were conducted by Cassel [50] and Ballal [51], as shown in Figure 2.26. Sun et al. [21] also measured flame speed for the combustion of iron as a function of the concentration for lean and rich mixture, which shows similar trend as the model predicted as can be seen in Figure 2.27.

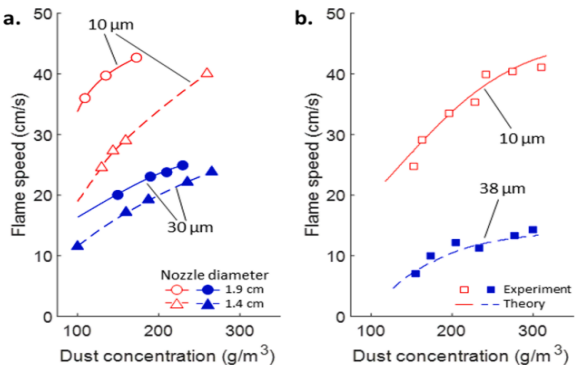

Figure 2.26: Flame speed with respect to fuel concentration in fuel-lean mixture of aluminium-air suspensions obtained by a. Cassel [50] and b. Ballal[51]. Reprinted from [29]

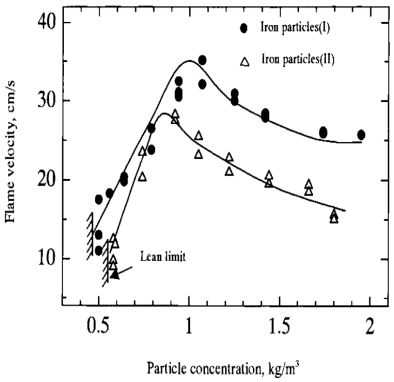

Figure 2.27: Flame speed as a function of the iron concentration for lean and rich mixture [21]

It can be noticed that the two studies on aluminium combustion of lean-mixture, have similar trends, with a dependence of the burning velocity (u_b) on fuel concentration (B) close to $u_b \propto \sqrt{B}$, as was predicted from the theoretical model. In a similar way, Goroshin et al. [52] measured the flame burning velocity of rich aluminium mixture, which fits with the model as can be seen in Figure 2.28.

Lomba et al. [34] also measured a plateau in the dependence of the burning velocity on the fuel equivalence ratio between 0,8 and 1,5 in the combustion of aluminium in air suspension. It can also be noted from Figure 2.28 that the burning velocity of fuel rich mixture is larger with higher oxygen concentration in the mixture. Indeed, in a diffusion regime, the fuel burning rate is dependent of the flux of oxygen to the particle, which is proportional to the oxygen concentration.

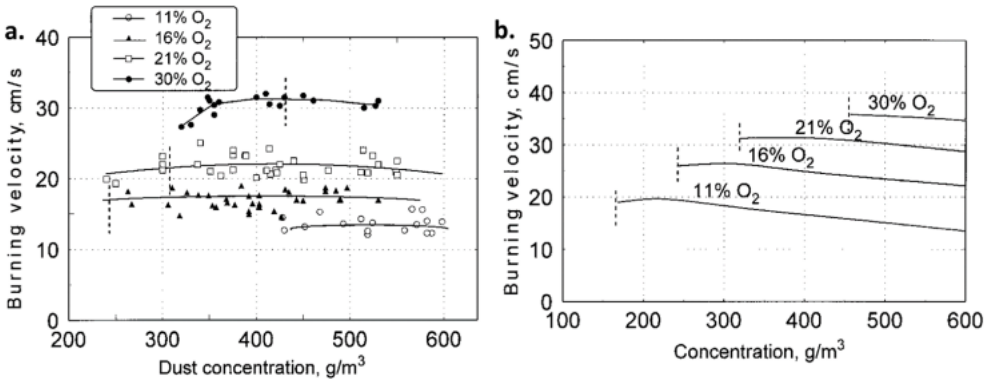

Figure 2.28: Burning velocity of aluminium fuel-rich suspension as function of the fuel concentration. a. from experimental results, b. calculated from model [52]

Hazenberg et al. [43] used a different model

Tang et al. [22] measured the flame speed of iron suspension in a micro-gravity environment, on board of a parabolic flight. They have tested 5 different fractions of powder, ranging from 3,3 to 32,5μm with different oxidising mixtures. They found out that the flame speed follows a $1/d$ law with respect to the particle diameter, as shown in Figure 2.29.

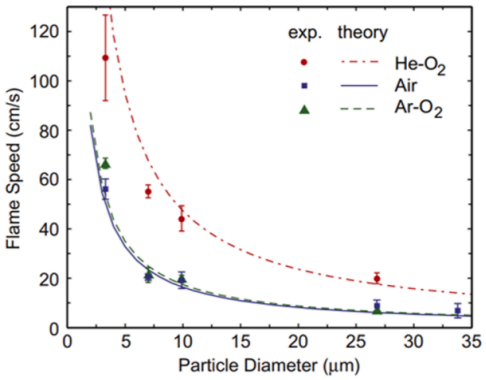

Figure 2.29: Experimental and theoretical comparison of iron flame as a function of the size [22].

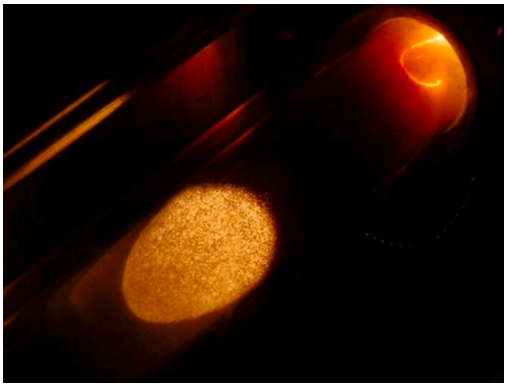

Figure 2.30: Iron flame under micro-gravity [29].

The increase of the burning velocity for smaller particles can be explained by the increase of the specific area that is available for the reaction [49].

Key points of this section :

- Near stoichiometry to rich: Burning velocity decreases when increasing particle size
- Rich-fuel mixture : small dependence of burning velocity the fuel concentration
- Lean-fuel mixture : dependence of the burning velocity (u_b) on fuel concentration (B) close to $u_b \propto \sqrt{B}$
- Rich-fuel mixture : Higher burning velocity with higher oxygen content

2.2.3.3 Particle and gas temperature in diffusion-limited regime

As stated before, metal powders burning in the diffusion regime will have particle temperature near the adiabatic stoichiometric flame temperature, while the gas temperature may be relatively colder, depending on the equivalence ratio of the mixture, as can be seen in Figure 2.31.

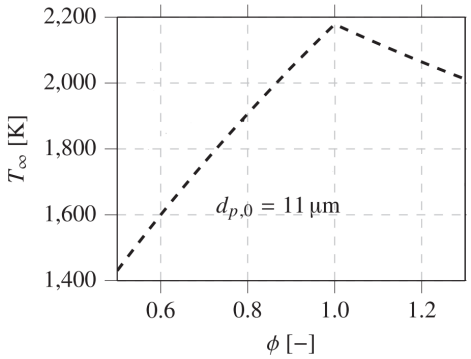

Figure 2.31: Gas temperature as function of the equivalence ratio [43].

Ning [53] measured the near-peak temperature of single iron particles as a function of the oxygen concentration and particle size. As can be seen from Figure 2.32, the temperature increases with increased oxygen concentration, attaining a plateau for high oxygen concentration. Moreover, larger iron particles have higher near-peak temperature. This is explained by the fact that there is less radiative heat losses due to a smaller surface-to-volume ratio than for smaller particles. The difference of temperature is less significant for lower oxygen concentration. It can be explained by the fact that radiative heat transfer plays a less significant role. Indeed, radiative heat transfer depends on the temperature, which will be lower due to a smaller oxygen concentration.

Key points of this section :

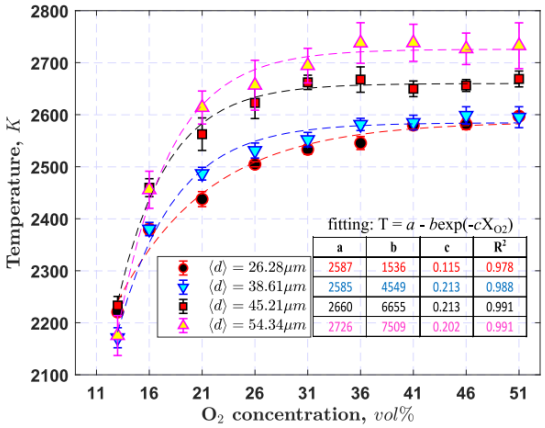

Figure 2.32: Iron particle temperature as a function of the oxygen concentration and particle size [53].

- Metal powder particles burning in the diffusion regime will have a temperature near the adiabatic stoichiometric flame temperature
- Gas temperature in a flame depends on the equivalence ratio
- The surface particle temperature increases with increased oxygen concentration before attaining a plateau
- Larger iron particles have higher peak temperature

2.2.3.4 NO_x emissions

The key element in the combustion of metal powders is that it does not produce any carbon dioxide or any other carbon-based pollutant such as soot, carbon monoxide or unburned hydrocarbons. That way, it is possible to achieve a sustainable cycle with zero green house gases emissions, if the energy used for the reduction process is clean. But combustion with air often produces other pollutants such as NO_x, SO_2 or solid residue, which are an issue for human health and environment pollution. Some after treatment processes exist in order to capture NO_x at the exhaust of most thermal engines, but decreasing emissions at the source helps avoiding too complex devices of such sort. The NO_x emissions produced by the setup build in the context of this thesis will be analysed in section 4.5. During the combustion with oxygen, several mechanisms intervene in the production of NO_x [54][55][26]:

- **The thermal mechanism (Zeldovich):** This is the main source of NO_x in almost all cases. The mechanism that describes this phenomena is the

following :

$$O_2 \rightleftarrows 2O \tag{2.4}$$

$$N_2 + O \rightleftarrows NO + N \tag{2.5}$$

$$O_2 + N \rightleftarrows NO + O \tag{2.6}$$

In this system, Equation 2.5 is the limiting reaction as the strong bond of nitrogen molecule need to be broken to react. Therefore, the most important parameter for this process is the temperature, as the rate of the reaction will increase exponentially with temperature. The residence time and the availability of oxygen also play a crucial role. It can be said that NO starts to form at 1600K and the residence time is in the order of seconds. If the temperature rises to 1800-2000K, a residence time in the order of milliseconds already produces a significant amount of NO.

- **Fuel-bound nitrogen mechanisms:** The NO is formed through the nitrogen that is already present in the fuel and that will react with the oxygen in the air. The fuel-bound NO can participate in a large part of the total NO_x production, as 20% to 90% of the nitrogen contained in the fuel can be converted in NO, depending on how the combustion takes place.

- **Fenimore mechanism (Prompt NO):** the NO generated by the Fenimore mechanism results from the radical CH which is formed during combustion of hydrocarbons by the following process :

$$CH + N_2 \rightleftarrows HCN + N \tag{2.7}$$

$$C_2 + N_2 \rightleftarrows 2CN \tag{2.8}$$

Where the HCN and CN compounds will eventually oxidize to NO via a complex mechanism that is outside the scope of this thesis. It is formed 'suddenly' in short residence time and under low temperature ($\sim 1000K$).It is considered the least important source of NO.

There is very little research that have been done on the subject so far. Eindhoven University published some results of NO_x emission measurements from the 100kW setup covered in section section 2.1 [26]. The results are shown in Figure 2.33.

Results show that the more iron is added to compensate the propane, the less NO_x is emitted from the burner. As the combustion temperature of iron is similar to that of hydrocarbons, one could first expect that NO_x emissions would be comparable to hydrocarbons, but results demonstrate otherwise. Among the

Exp.	Description	NO, ppm	NO2, ppm
1	Propane flame, heat up burner	94	1
2	Propane (large gas flow) + iron	59	0
3	Propane (gas flow is less than in Exp. 2) + iron	40	0
4	Propane (gas flow is less than in Exp. 3) + iron	24	0
5	Propane (gas flow is less than in Exp. 3) + more iron (than Exp. 2-4)	17	0

Figure 2.33: NO_x emissions from 100kW burner setup [26].

different mechanisms that produce NO_x cited before, the last two involve the hydrocarbon fuel itself, and are therefore not relevant in the NO_x emissions for the combustion of metals. Indeed, no CH radicals are formed during the combustion of iron, and the fuel does not contain any nitrogen. Still, the thermal NO is often the most dominant form of NO, and the two other mechanisms being irrelevant, does not justify such differences in NO_x emission for similar burning temperatures. They have suggested a model where hydrogen also plays an important role in the formation of NO_x, as it helps increasing the number of oxygen radicals available, which are crucial in the Zeldovich process in Equation 2.5. Results from the model can be seen in Figure 2.34.

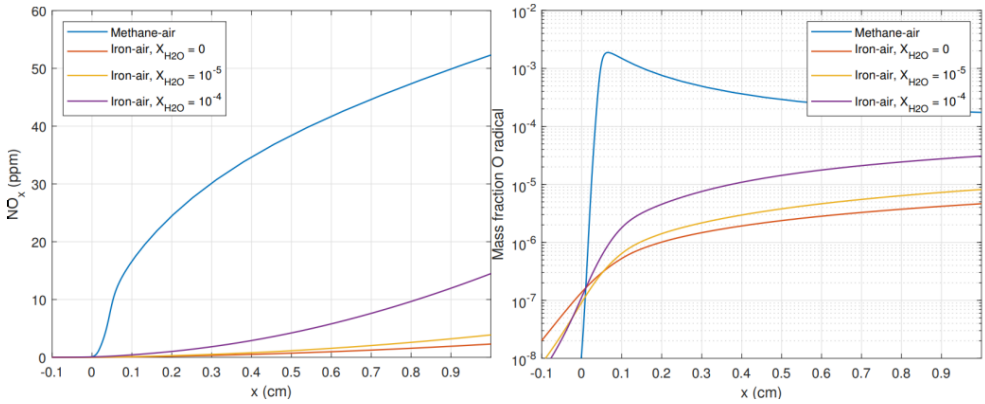

Figure 2.34: Influence of the concentration of water added to the combustion on the a) NO_x production and b) O-radicals formed, as a function of the flame front. Note the logarithmic scale for the O-radical graph. [26]

It can be seen that during the combustion of iron with air, the amount of O-radicals available is significantly lower than for a methane flame. The fraction of radicals increases when increasing the H_2O content in the air, and so does the NO_x emission. This shows that, from this model, the presence of hydrogen atoms also plays an important role in the emissions of NO_x.

Wiinika et al. [19] used a small-scale entrained-flow reactor to model the en-

vironment of a pulverized coal (PC) burner. Which is a tube furnace operating at 1200°C, covered in section section 2.1. They studied the behavior of pulverized sponge iron (PSI), a product of the direct reduction of iron oxide, as a potential replacement of PC in coal applications. During the combustion tests of two types of PSI and coal, they have measured the emissions of CO_2, NO_x, CO, SO_2 and solid residue.The experiments were conducted with an equivalence ratio of 0,5 and a thermal power of 310W in each cases. Results are shown in Figure 2.35. As expected, no trace of CO and CO_2 were detected during the combustion of PSI. Concerning the NO_x and SO_2 emissions, it has been shown that using PSI instead of coal, NO_x reduced from 500 to 20 mg/MJ_{fuel}, in other word, emissions 30 times lower than with coal. For the case of SO_2, emissions reduced from 230 to 1-7 mg/MJ_{fuel}, depending on the type of PSI, with a reduction by a factor more than 30.

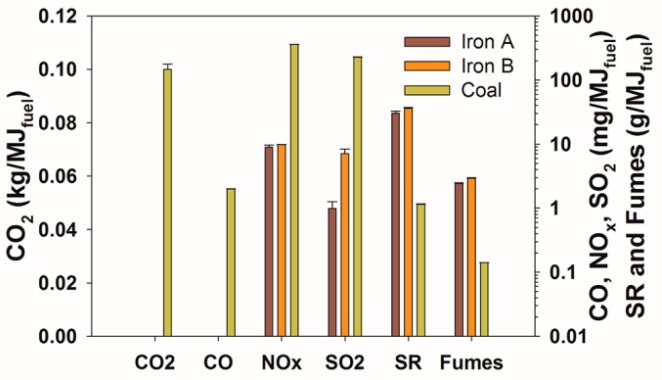

Figure 2.35: Results of combustion tests comparing 2 types of PSI and coal. Solid residue (SR) and fumes were defined as particles above and below 10μm respectively [19].

Once again, the significant decrease in the production of NO_x can be explained by the fact that during the combustion of PSI, only the thermal mechanism is relevant for the combustion of NO_x, which requires high temperature (above 1600°C) and the availability of oxygen. Both condition were met during the tests. Also, no CH radicals can be formed and the iron does not contain any nitrogen, as opposed to the coal in this study where it represent 1,33% of the composition. On the other hand, NO_x emissions from the PC combustion in the small scale EFR are similar to the one in the PC boilers, which indicates that the experimental conditions of this study are relevant.

Garra et al. combusted magnesium particles inside a combustion chamber

[56]. They used two ranges of powder : 20-50 μm and 50-70μm. They measured that the NO_x emitted by the combustion was higher for the 20-50μm than for the 50-70 μm Mg fraction, with respectively 4300 $\pm$ 200 $mg/(N)m^3$ and 1100 $\pm$ 140 $mg/(N)m^3$. Magnesium particles are highly reactive and burn accordingly to the $t \sim d^2$ law. The larger the particles, the longer the particles will burn, so that the temperature in the combustion chamber will be more uniform and thus with a reduction of the peak gas temperature, reducing as well the generation of NO_x. Wiinika et al. normalized this value with respect to the energy produced and found a value of 125 $\pm$ 16 mg/MJ [19]. Which is more than 6 times superior to the value of 20 mg/MJ that they found in their study for the combustion of iron. This can be explained by the fact that magnesium burns at a significantly higher temperature than iron. The production of thermal NO is thus much larger as the rate of the Zeldovich process increases exponentially with temperature.

Laraqui et al. measured the NO_x production of magnesium burned inside a combustion chamber [57]. They have varied the equivalence ratio from 0,29 to 0,98. The results have been normalized with the minimum and maximum NO_x emissions that a commercial gasoline engine produces when functioning with the power. The results of this study are found on Figure 2.36.

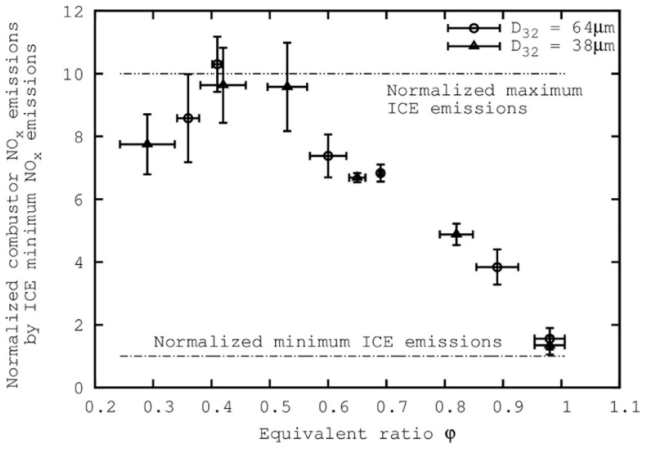

Figure 2.36: Normalized NOx emission with respect to the equivalence ratio [57].

Results show a parabolic trend in the emission of NO_x, with a maximum for an equivalence ratio of around 0.4. At that equivalence ratio, the temperature is still high enough and offer a stable chemical conversion for the production of NO and NO_2 respectively. They tested two different size ranges of particles, one with mean diameter of 38μm and the other with 64μm. They did not notice any significant differences in NO_x production between the two ranges as the difference in flame

temperature is not sufficiently important, with the temperature of the larger range being slightly higher than the one of the lower range. The thermal pathway of NO_x production is therefore not really affected by the size range of particle for the combustion of magnesium. The measured NO_x emission is comprised between the highest and lowest emission of benchmarked ICE engine, which is promising when considering such early phase of development .
Key points of this section :

- Metal combustion only emits NO_x via the thermal mechanism
- Significantly lower NO_x emission when combusting iron powder than hydrocarbon fuel.
- emission of NO_x particles will be significantly larger when burning magnesium than iron, due to the much higher temperature which favors the thermal pathway
- Size of magnesium particles appears to have no influence on NO_x emissions
- Presence of hydrogen in hydrocarbons may play an important role on the formation of O-radicals, which are crucial in the thermal mechanism

Chapter 3

Experimental design of an iron combustion setup

The objective of this section is to present the development process of an experimental iron combustion setup. The key steps in the design process will be presented, as well as the main difficulties encountered throughout the development of the burner. The whole system is composed in three parts. First, a airflow system will provide air at a given pressure and flowrate. Secondly, the airflow will be mixed with the iron powders in a feeding system. Lastly, the air and iron mixture will be burned in the combustion system. A representation of the different parts is shown in Figure 3.1

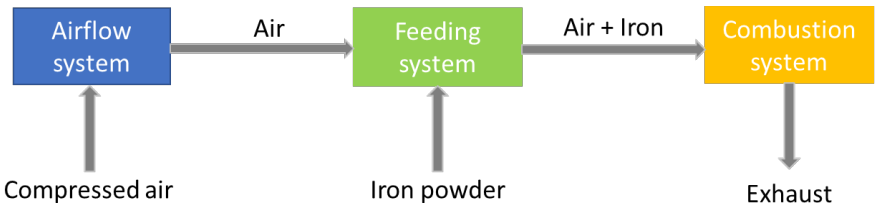

Figure 3.1: Schematic representation of the burner.

3.1 Air and iron flowrates

In order to design the metal burner setup, extreme cases scenario need to be identified to set the limit of operating condition.

- The first case concerns the lower limit and is achieved when producing a 3kW flame with an equivalence ratio equals to 1. This set of parameters was chosen for the minimum air flowrate that can achieve a efficient fluidization.

- The second concerns the upper limit and is reached when producing a 5kW flame with an equivalence ratio equals to 0.6. Those parameters were chosen as the limit at which the flame can be contained safely.

Here is the calculations needed to find out the volumetric flowrate of iron and air. The combustion of iron in air is given by the following equation :

$$Fe + \frac{3}{4}O_2 \longrightarrow \frac{1}{2}Fe_2O_3 - 413kJ/mol \tag{3.1}$$

The molar flowrate of iron needed is therefore :

$$\dot{n}_{Fe} = \frac{P_{target}}{Molar heat of combustion} \tag{3.2}$$

	Power [kW]	Iron molar flowrate [mol/s]
Lower limit	3	0,0073
Upper limit	5	0,0121

Table 3.1: Molar iron mass flowrate for operating limits.

Now considering the molar mass and the bulk density calculated experimentally, the mass and volumetric flowrates of iron are given by :

$$\dot{m}_{Fe} = \dot{n}_{Fe} \cdot M_{Fe} \qquad \dot{V}_{Fe} = \dot{m}_{Fe} \cdot \rho_{bulk} \tag{3.3}$$

With $M_{Fe} = 55.85g/mol$ and $\rho_{bulk} = 4249.53kg/m^3$, the values found in both case scenarios are gathered in Table 3.2

	Power [kW]	Molar flowrate [mol/s]	Mass flowrate [g/min]	Volumetric flowrate $[cm^3/min]$
Lower limit	3	0,0073	32,46	7,64
Upper limit	5	0,0121	48,68	11,46

Table 3.2: Iron flowrates for operating limits.

Concerning the flowrate of air, Equation 3.1 states that for 1 mole of iron, $\frac{3}{4} \cdot \frac{1}{\phi}$ moles of dioxygen is consumed. The moles of air used can be found with $n_{air} = n_{O_2} \cdot \frac{1}{0.21}$. The molar flowrate of air is therefore given by :

$$\dot{n}_{air} = \dot{n}_{Fe} \cdot \frac{3}{4}\frac{1}{\phi}\frac{1}{0.21} \tag{3.4}$$

At 0°C and 101325 Pa, one mole of gas occupies 0.0224 $m^3/mole$. The following table summarizes the different volumetric flowrates for the two limit cases scenario.

	Power [kW]	Volumetric flowrate iron $[cm^3/min]$	Equivalence ratio	Volumetric flowrate air $[Nm^3/h]$
Lower limit	3	5,73	1	2,09
Upper limit	5	9,55	0.6	5,81

Table 3.3: Volumetric flowrate of iron and air for operating limits.

Those calculations have allowed to identify the boundary operation limits of the setup.

3.2 Airflow system

The air needed for the setup is provided by a 9bar compressed air network. Therefore, it first needs to be extended through a pressure reducer. The combustion will occur around the atmospheric pressure. So the pressure reducer will be set to around 1.5 bars in order to compensate the pressure loss of the air flow in the feeding system before attaining the combustion chamber, which was estimated to be enough. After leaving the pressure reducer, the air flow goes through a rotameter that will measure the volumetric air flow at normalized condition. A control valve is used between the two devices to control the flow. The whole air system is shown in Figure 3.2

3.3 Feeding system

The main difficulty of this setup is the realization of the feeding system. Indeed, the feeder must be able to mix air with iron powder in an effective manner. The main difficulty lies in producing very low iron flowrate. Indeed, given the bulk density of iron powder, the volumetric flowrate is ranging from $7,64cm^3/min$ to $11,46cm^3/min$ for the chosen power outputs. In order to create that mixture of air and iron, the powders will have to fluidize.

3.3.1 A word on fluidization theory

The process at which fine solids are transformed into a fluid-like state through contact with a gas or liquid is called fluidization. When designing a setup to burn

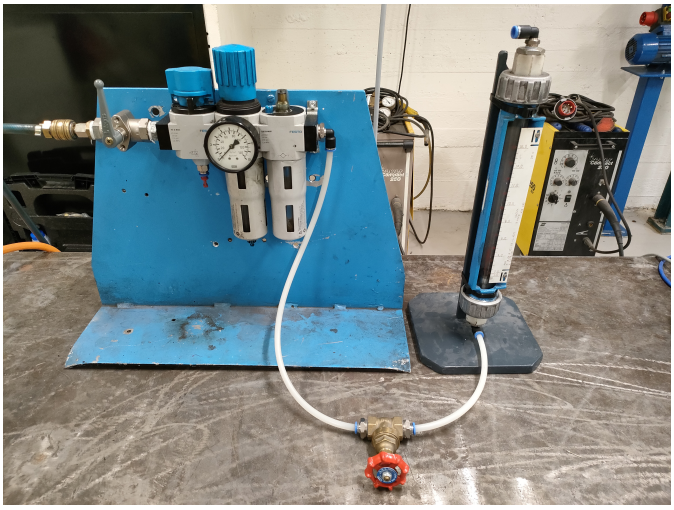

Figure 3.2: Airflow system used in the combustion setup.

metal powders, one of the main challenge is the fluidization of the particles. Indeed, to produce a metallic flame, a mixture of metallic powders and oxidizing gas must first be generated. It will be covered in this section the important theoretical background concerning the fluidization that have helped the design of the burner.

3.3.1.1 Terminal velocity of a particle

It is possible to distinguish several types of fluidization regime within a gas-solid system, depending on the velocity of the flow in contact with the particles [36]. Listed hereunder by order of increasing velocity.

- Fixed regime.
- Bubbling regime.
- Turbulent regime.
- Pneumatic regime.

In the first three regimes, there is no large-scale transportation of the particles with the gas. However, this is not the case for the pneumatic regime for which the discussion will be focused on. Pneumatic transport occurs when the gravitational force balance the buoyancy and drag force caused by the moving fluid, as shown in Figure 3.3.

The fluid velocity at which the pneumatic transport is attained is called terminal velocity. For high Reynolds number, the terminal velocity of a spherical particle is given by the Newton's Law :

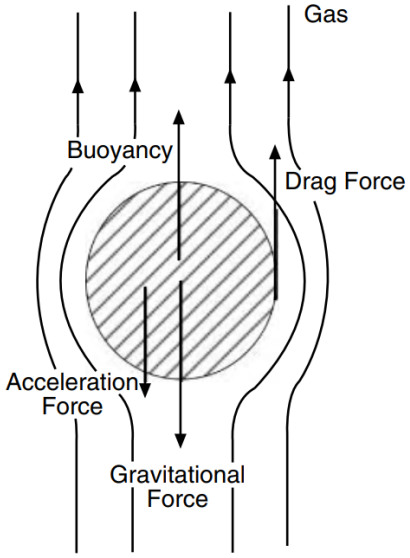

Figure 3.3: Schematic of the force balance on a particle in a moving fluid [36]

$$V_t = 1.74\sqrt{\frac{gD_p(\rho_p - \rho_g)}{\rho_g}} \tag{3.5}$$

Where :

- V_t = terminal gas velocity [m/s]
- D_p = the particle diameter [m]
- g = gravitational acceleration $[m/s^2$
- ρ_g = gas phase density $[kg/m^3]$
- ρ_p = particle phase density $[kg/m^3]$

Under this velocity, the particle will not be able to be transported by the moving fluid. It is therefore necessary to ensure that each part of the setup has a higher air velocity than the terminal velocity of the largest particles of the sample, preferably including a safety factor.

3.3.1.2 Particle classification

A classification of the particles have been performed by Geldart [58] under four different groups that are classified with respect to their size and the difference

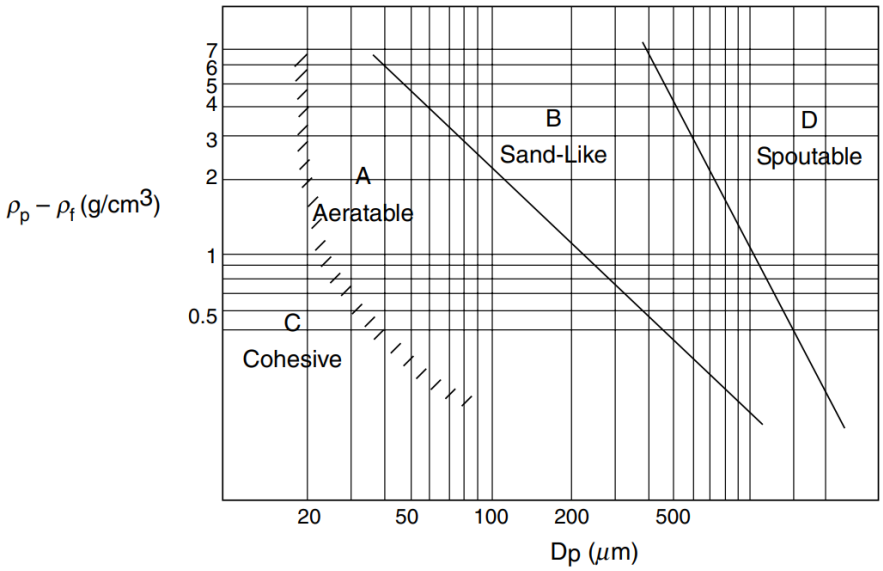

Figure 3.4: Graphical powder classification as function of particle size and density [36]

Groupe A, Aeratable	Particles are easy to fluidize and are in the range of 20 to 40μm (if $\rho = 7000kg/m^3$)
Groupe B, Sand-Like	Particles fluidize well and are in the range of 40 to 400μm (if $\rho = 7000kg/m^3$). Bubbling regime appears at the minimum fluidization velocity.
Groupe C, Cohesive	Concerns mainly particles under 20μm. These powders are difficult to fluidize because the gravitational force is comparable to the inter-particle forces.
Groupe D, Spoutable	Particles larger than 400μm (if $\rho = 7000kg/m^3$) that require high flow velocity to fluidize

Table 3.4: Particle group classification

between the density of the particle to that of the fluidizing gas. The groups are represented in Figure 3.4 and described in Table 3.4:

In the application of metal powders as energy carrier, only the first three groups are relevant. Among them, it is very preferable to use particles from group A or B, as fluidization complications emerge with group C. Indeed, particles from this group are subjects to cohesive forces which makes them very difficult to fluidize with a gas. The main attractive force is the Van der Waals [59]. Electrostatic forces can also play a significant role in the fluidization.

3.3.2 Feeding system state of the art

A few design have been thought about for this purpose, inspired from the literature.

- **Gravity feeder** : The powder is stored in a tank above a controlled valve, the powder can then fall under is own weight in a compressed gas flow thanks to gravity. The controllability of the feeder is done by opening more or less the control valve. In order to measure the mass flowrate, the tank can be suspended under a scale. This system is used in particular by the *TEAM SOLID*, from the Eindhoven University. It has been tried during the design process and has one main problem. The powders do not fall by themselves as they lack viscosity. This solution need to be completed by a vibrator that will produce some slight movement and make the powders fall. In addition to make this simple feeding solution much more complex, the system become less precise and more difficult to control.

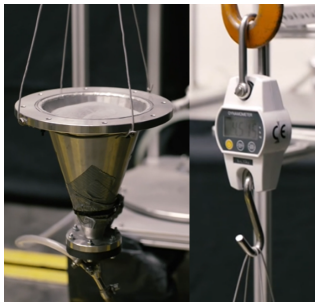

Figure 3.5: Gravity feeder coupled with vibrator suspended at scale [30]

- **Powder dispenser :** This is certainly the most effective way to create an aerosol of powder and possess a large range of operating condition. Indeed, it can produces mass flowrates of powder from 100g/h to 6kg/h. It can also be used with a wide range of granulometry with particles size from 0.1μm up to 200μm. This system notably used at the burner setup situated at the *Université of Haute-Alsace*, Mulhouse [57]. The main disadvantage of such equipment is the economic value, with a price of around 12.000€ for the device used here above.

Figure 3.6: PALAS powder aerosol generator [60]

- **Venturi injectors:** Those are devices that use the Venturi effect, which is a physical principle that causes a fluid to increase its speed when going through a constricted area. As the fluid is increasing speed, the pressure drop and it will create a depressurisation inside the nozzle and will suck metal powder to the fluid through the suction chamber. This system was used at the *Centre National de Recherche Scientifique*, Orléan [34]. But was later replaced by an aerosol generator mentioned here above [61]. Indeed, this system also need a powder activator in order to help fluidize. For example, the CNRS setup also includes a stirred powder reservoir, which will reduce the precision of the solution.

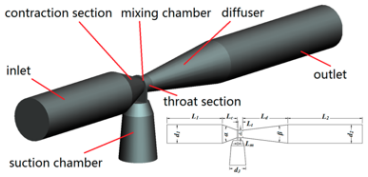

Figure 3.7: Venturi Injector [62]

- **Syringe type feeder** : The powder is first stored in a cylinder tank. A linear actuator will move a syringe plunger that will push metal powders upward. An air entrance is situated in the wall of the cylinder, with a low section in order to have high speed velocity at the inlet. As the powder is moving up, it is fluidized by the fast moving air and driven away at the top output. For example, this system is used at *McGill University* with the scheme shown in Figure 3.8. The main disadvantage of this kind of system is the duration of the experiment, as it will be defined by the quantity of powder that can be stored in the cylinder and the powder flowrate required.

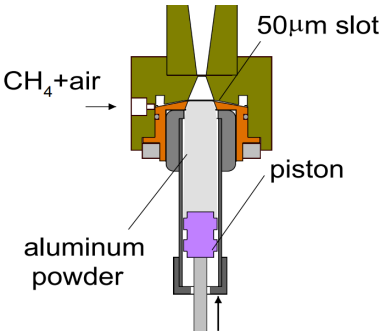

Figure 3.8: Syringe type feeder used at *McGill University* [63]

3.3.3 Feeding system solution

The chosen design was inspired by the work done at *McGill University*, using a syringe type feeder. Indeed, this design shows a fair trade-off between the simplicity of the design and the precision achieved. It was also easily built as most parts were already available at the CREDEM platform. It is constituted of mainly two parts: the feeder and the linear actuator. The feeder was first modeled on the software

Solidworks and then 3D printed. It feeder has been through two well separate models, each with a multitude of different versions. The evolution of the initial model of feeder is shown in Figure 3.9

Figure 3.9: Evolution of the first model of feeder.

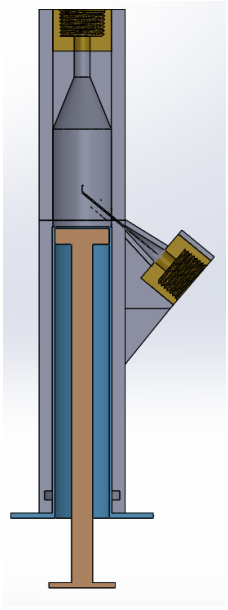

Figure 3.10: Feeder model 1

The particularity of both model of feeder, is that they include directly a syringe tube inside of the cylinder. This choice was made for two reasons. Firstly because of the rough surface of the 3D print, which did not ensure the airtightness between the plunger tip of the syringe and the wall of the cylinder. Secondly, it provides a simple way to load the feeder in powder, as the syringe tube can be removed from the cylinder as needed in a simple manner. In the first model of feeder, the air entrance is situated on one side of the main cylinder through an air knife of 0,5μm, as can be seen in Figure 3.10. As the powder is moving upward, it mixes with air and the mixture goes out by the top of the feeder, to be burned in the combustion chamber. More information on this type of feeder and the several tests that have been done to validate this part can be found in appendix A.

Unfortunately, in the last stage of validation of the feeder, this model of feeder showed some problems concerning the feeding rate of powders. Indeed, the particles were leaving the feeder by small packages every one or two seconds, which produced inconsistent flames. This particularly was not noticed during the cold mode test

Figure 3.11: Evolution of the final version of the feeder.

because measurement were taken with 10 seconds intervals. This problem may be due to the air knife in the cylinder, which may not have been small enough to ensure high flow velocity.

Therefore, a second model had to be designed, which also went through several iterations as can be seen . This model also include a syringe tube that allows a plumber to move vertically, but now the whole air flow is moving horizontally, as can be seen Figure 3.12.

In order to ensure the permeability between the syringe tube and the cylinder, a O-ring joint is used in the groove that can be seen in Figure 3.14. The initial diameter of the the tube syringe, where the powder is stocked is 22mm. A shrinkage of this diameter is performed at the top of the syringe tube. This has been done for two reasons, the first one is to reduce the section of the air canal above the powders, because its width is equal to that of this diameter. Doing so, the air velocity will be greater to ensure a good fluidization, while keeping the same quantity of powder in the reservoir, at the expense of a larger power needed at the motor. Also, the powder will have a higher vertical velocity at the tip of the cylinder, so that the air will not *dig* in the powder stock. Moreover, as you can see in Figure 3.13, a transparent plexiglass plate is fixed above the fluidization zone in order to have an optical control on the process. Lastly, it can be seen that the feeder is not symmetrical. Indeed, the outlet section is larger than the inlet section so that the air will not tend to dig into the powder reservoir.

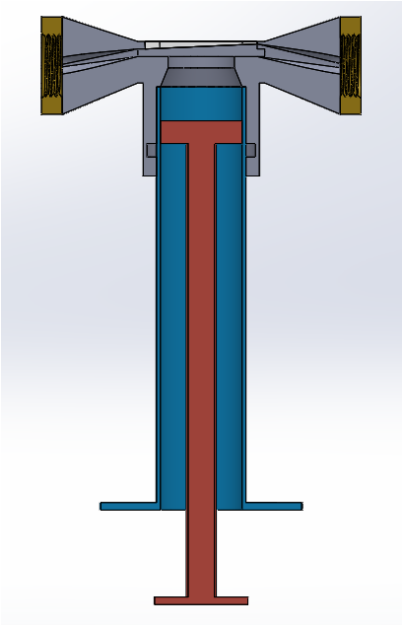

Figure 3.12: Final feeder cut. Syringe tube in blue, plumber in red.

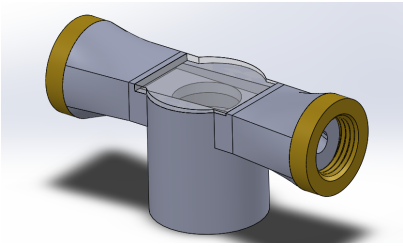

Figure 3.13: Final Feeder

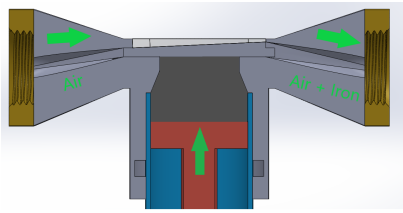

Figure 3.14: Final feeder cut 2. Dark grey is the iron powder

Concerning the linear actuator that will push the powder upward, the system must be able move the syringe plunger upward with a low speed. Indeed the inner diameter of the syringe tube measures $2.2cm$. Given the minimum volumetric flowrate of iron powder needed of 7,64 cm^3/min, obtained in Table 4.2, the actuator must achieve a minimum vertical linear speed of :

$$\frac{7.64}{\Pi\frac{2.2^2}{4}} = 2cm/min = 0.33mm/s \tag{3.6}$$

The speed of the actuator needs to be very precise, constant and easily controllable as it will drive the different equivalence ratios for the experiments. The choice has been made to use a high precision lead screw slide, shown in Figure 3.15, coupled with a stepper motor. The shaft of the stepper motor is directly connected to a lead screw. As the lead screw is turning, it will convert the rotational motion into linear motion and will move the slide. The slide will be connected directly to the syringe plunger that will then move the metal particles upward. With this feeding system, the mass flowrate of powder will be monitoring by controlling the RPM of the stepper motor, using the *EPOS STUDIO* software. The screw slide has a pitch of 1mm and a stroke of 10cm.

Figure 3.15: Lead screw slide

Given those parameters, the stepper motor much achieve a minimal speed of 20rpm. In order to choose the suitable stepper motor, experiments have been done to estimate the maximum linear strength that the motor has to produce. This maximum force occurs when the syringe tube is loaded at its maximum with metal powder and when it has to counteract the static friction of the powders inside the tube in addition to the weight of the powders themselves, which can be translated as :

$$F_{\text{max}} = F_{\text{static friction}} + W_{\text{powders}} \tag{3.7}$$

The static friction force has been estimated by carefully adding weight to the top of a fully loaded syringe and see from what charge the syringe tube start to move with respect to the plunger. The simple experiment is shown in Figure 3.16. The weight associated with this mass can be estimated as the static friction force.

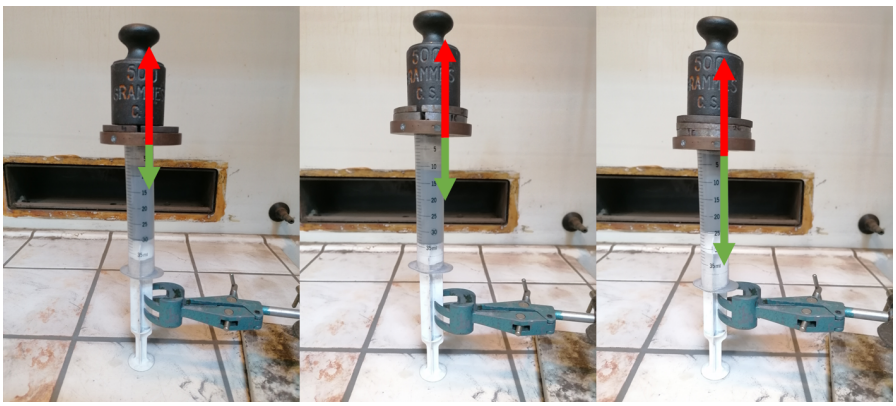

Figure 3.16: Simple experiment to estimate the static friction force inside the syringe tube.

The experiments shows that the tube start moving with a mass of 1.02kg. Also during the experiment, the powder inside the tube has a total weight of 0.105g. The maximum linear force that stepper motor has to produce is therefore ;

$$F_{max} = (1.02 + 0.105) * 9.81 \approx 11N \tag{3.8}$$

When considering a safety factor of 4, the stepper motor needed must be able to produce a linear force of minimum 44N. A motor available at the CREDEM platform met the requirements and was then connected to the lead screw slide. A support was build in order to hold the stepper motor and the slide vertically. The piece connected to the slide that will push the syringe plunger was also build. The whole assembly is shown in Figure 3.17.

3.3.4 Validation of the feeding system

The feeding system must be able to fluidize metal particles in an efficient manner. More specially, it has to produce precise, constant and easily controllable equivalence ratio in order to make analysis based on the tuning of this parameter. In order to conduct experiments, a "cold mode" setup was built. It contains the components needed for the air flow system and the feeding section. But the outlet of the feeder is connected to a special recovery system that will capture and stock the metal particles after being fluidized. This recovery system is situated above a scale in order to measure the mass of powder that is getting fluidize over time. This setup is shown in Figure 3.18.

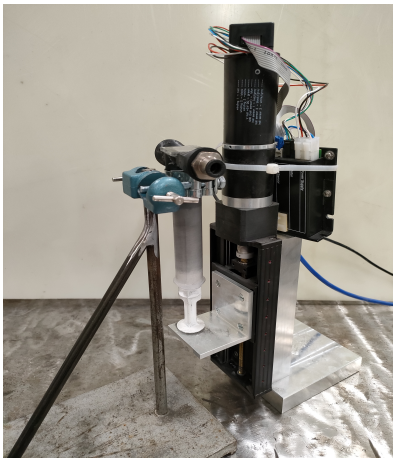

Figure 3.17: Feeding system

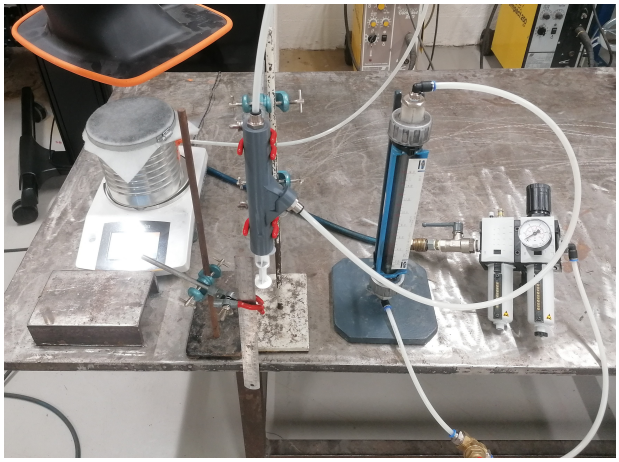

Figure 3.18: Setup with cold recovery system using first model of feeder

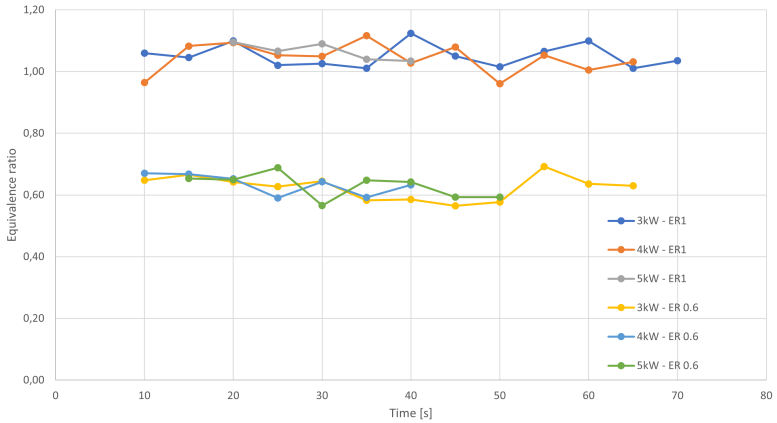

Figure 3.19: Equivalence ratio as a function of time for different set of parameters.

The cold mode recovery setup is constituted of a thin metal can in which the mixture of air and powder enters from an opening on the side of the can. The outlet is done on the top of the can by going through a filter. The recovery of particles happens with the help of two separate methods. The first one is by gravity. Indeed, as the fast moving flux of air and powders enters the metal can, their velocity is reduced significantly thanks to the mass conservation principle. This velocity becomes lower than the pneumatic transport velocity and the particles start to fall down at the bottom of the can where they are stocked. Unfortunately, the gravity recovery solution loss efficiency for particles smaller than 40μm [64]. This is why it has to be coupled with the second method which is simply the capture by the filter. A filter of class G4 is used and has been chosen with the help of a selection chart available in appendix C. Recovery rate of more than 99% were obtained using this system.

The feeding system have been tested in cold mode to ensure that it could reproduce the different equivalence ratio needed for the analysis. Measurement of the mass recovered were taken every 5 seconds, and no particle "packages" have been observed. Results are shown in Figure 3.19 and Table 4.2.

Power [kW]	Target equivalence ratio	Mean equivalence ratio	Average error from mean equivalence ratio
3	1	1,051	2,8
4	1	1,036	3,6
5	1	1,065	2,1
3	0.6	0,625	5,0
4	0.6	0,635	4,1
5	0.6	0,630	4,7

Table 3.5: Volumetric flowrate for the two limit cases scenario.

We can see that the measured equivalence ratio is always a little higher than the target value. This shift can easily be corrected by calibrating the speed of the motor accordingly. Therefore, the most important parameter to look into is it the average error from the mean equivalence ratio. We can see that the maximum average error is 5%, and that the range of variation was calculated to be $\pm 7.5\%$ with a confidence level of 95%. Which is acceptable to have relevant analysis on the equivalence ratio. In comparison, the setup used at the CNRS center in Orléan, which uses a venturi injector coupled with a scale, has an range of variation of 8% with the same confidence level [34].

This part of the design process was the most time consuming part of the project. In total, over 70 cold mode tests were performed during the feeder design process, using 8 different feeder iterations. Each iteration went through a modeling and 3D printing phase. Also, a agglomeration problem was encountered during that process that further complicated things. It is explained in more details in section appendix B, with attempts to identify the problem, which were unfortunately unsuccessful.

3.4 Combustion system

Once the the mixture of air and iron is formed, it is entrained in the combustion chamber to be ignited. There, the flux goes out through a burner head and is ignited. The choice has been made to use simple metal pipes as a burner head, and to ignite the particles thanks to a secondary hydrocarbon flame. Different designs have been tested in order to have the most stable and efficient flame, i.e. that contains the less unburned possible.

- The first setup was realised using a 7mm-diameter pipe and a blowtorch as a way to ignite the particles. The first iron flame realized in the context of this thesis can be seen in Figure 3.20. The setup was placed inside an aluminium flexible ventilation duct for safety purposes. This was the first tryout of creating an iron flame, on a much non-optimized setup. Indeed, the blowtorch was not properly fixed and the secondary flame was highly impacted by turbulence and was difficult to position in an efficient way to let the particles go through it. Also, visual observation of the flame was complicated. Even though, the first attempt was successful at creating a small iron flame, which was encouraging for the upcoming versions of the setup.

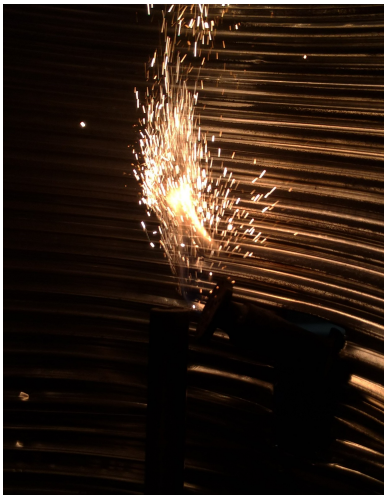

Figure 3.20: First iron flame obtained.

- The second setup used a plexiglass cylinder as protection. That way, it was much easier to observe the flame and draw conclusions from it. The feeding pipe used was upscaled to a 9mm diameter and possesses a longer length in the purpose of laminating the mixture. Also, the setup used a more powerful blowtorch, as can be seen in Figure 3.21.

Figure 3.21: Second iteration of the combustion system.

This flame was much more stable than the previous one, and it can be seen that more particles were getting ignited. However, the flame has a flat profile, as shown in the side view. It can be explained by the fact that the flux

emitted by the blowtorch was too powerful and coming only from one side of the powder mixture, which influences the efficiency of combustion.

- The next setup uses a flame ring as igniter. Using this system, the powder mixture can be ignited from all sides equally effectively. This design was inspired by the work done by Team Solid on their 20kW flame burner, presented in section 2.1. It consists of a steel pipe bent to the desired shape, and perforated with 1mm- diameter holes every centimeter. The ring is then connected to a propane tank from which it is possible to tune the flame intensity. Also, this is at that setup iteration that the "package problem" from the initial version of the feeder was discovered. Indeed, as shown in Figure 3.22, which highlight the strong fluctuations occurring during the combustion every few seconds.

Figure 3.22: Two pictures of the same flame taken one second apart.

- The fourth iteration of the burner contains a much wider nozzle with a diameter of 18mm. It has been tested for two reasons, firstly to reduce the flow velocity of the mixture at the nozzle, so that the particles may spent more time near the propane flame zone to get ignited, and secondly for the particles to be nearer to the individual propane flame. Images of the flame created with this setup can be found in Figure 3.23. Falling ignited and non-ignited particles can be observed. It may be due to the flow velocity of the mixture being too low because of the wider nozzle.

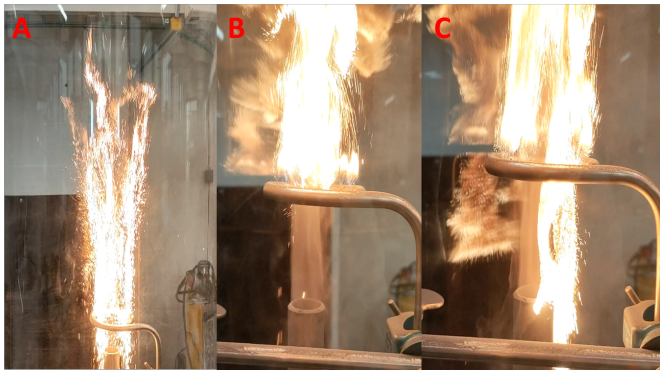

Figure 3.23: Flame obtained with the fourth iteration of the burner. Pictures B and C taken a few frames apart.

- The fifth iteration of the burner possesses a burner head smaller than the previous one with a 11mm inner diameter. The igniting ring have been reduced so that the iron and air mixture are closer to the propane flames. In addition, the temperature in the axial position is assumed to be higher. The flame produced by that setup is shown in Figure 3.24. This setup produced a flame looking more powerful than the previous iterations and concluded the setup design, which can be seen in Figure 3.25.

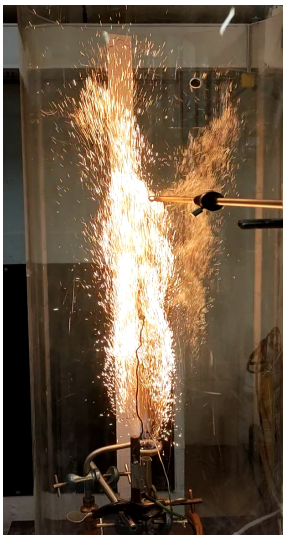

Figure 3.24: Flame obtained with the fourth iteration of the burner.

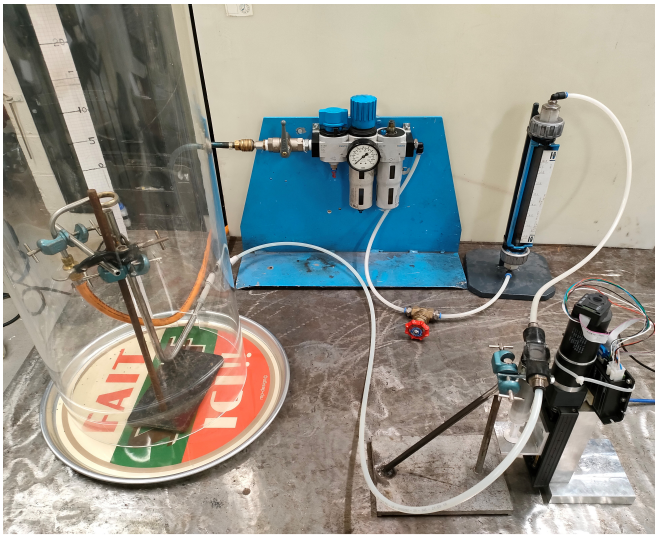

Figure 3.25: Full iron powder setup designed at UCLouvain

Chapter 4

Test, results and discussion

4.1 Critical parameters

Some critical parameters that will influence the combustion can potentially be tuned while using the setup designed in the context of this thesis. There are cited hereunder.

- **Power:** this is one of the main parameters and is proportional to the size of the flame. It is controlled by the speed of the stepper motor using a software.
- **Equivalence ratio:** it represents the proportion of air with respect to quantity of the metal fuel. It is modified by adjusting the air flowrate using a control valve, with the value of the air flowrate showed on the rotameter. It will also influence the flow velocity if using the same burner nozzle.
- **Particle size:** this is another critical parameter that influences highly the combustion behavior of the metal. It is modified by simply loading another powder granulometry in the syringe tube of the feeder.
- **Secondary flame:** its purpose is to ignite the metal particle and can be tuned by controlling the pressure valve of the propane tank.
- **Flow velocity at nozzle:** it affects the delay time that the particles spend in the ignition zone, and is also controlled by the equivalence ratio. To change the flow velocity without modifying the equivalence ratio, it will be necessary to swap the burner tube with another one of a different diameter.

The discussion will not focus on each critical parameter but some of them will be taken into account in the different discussion points here below.

4.2 Influence of propane secondary flame

In the designed burner, the iron particles are ignited using a circular propane flame. It is then important to determine the influence of this flame on the combustion behavior of the metal powder. In Figure 4.1, one can notice the strong dependence of the propane flame power on the iron flame power, since the same mass flow of iron is supplied in the 3 cases.

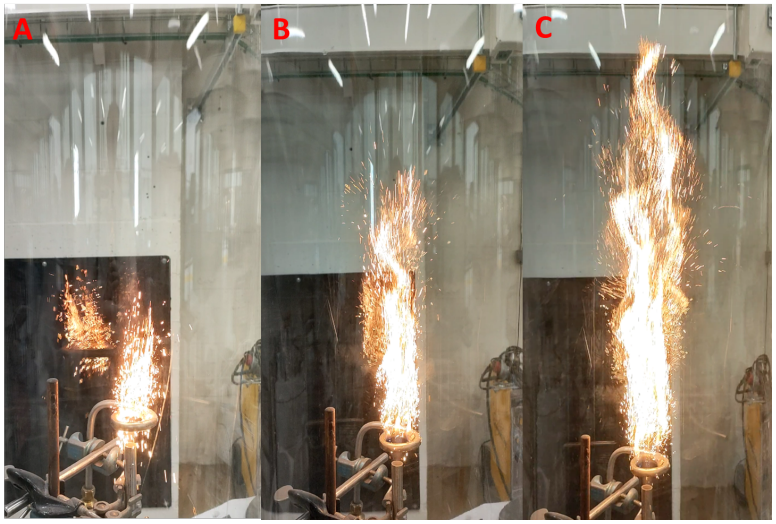

Figure 4.1: Influence of the intensity of the propane flame on the iron flame for the same iron mass flowrate provided for each test.

This can be explained by a larger zone with high temperature, which leads to a longer delay time for particles to ignite. But as some particles still ignite, it could be explained by the fact that ignition temperature of particle suspension is dependant of the particle diameter, as shown in Figure 2.15. Therefore, smaller particles will tend to ignite more easily than larger particles for a same temperature.

Also, if reducing the propane flame when the iron flame is well establish, the iron flame will decrease proportionally to the propane one, eventually to the extinction of the flame if no more propane is supplied. It means that in this setup, the iron flame cannot be self-sufficient and that an ignition flame must always be present. Moreover, all experimental iron flame in the literature use either an external heat source or a gaseous hydrocarbon fuel already mixed with iron before ignition. This is not the case for aluminum and magnesium, both of which have been observed to be able to stabilize the flame by themselves [34, 31]. Also, both of these metals have much higher burning temperature than iron. This suggests that once the

flame is establish the heat produced by the combustion of those particles is enough to not need an external heat source. Also, it could show that radiative heat transfer may play a role in the preheating of the particles before ignition.

4.3 Designed burner setup as an analysis tool

Effort have been made to design a feeding system able to efficiently produce iron-air mixture in a reasonable range of equivalence ratios. During some experiments, an attempt to utilize this functionality to analyze combustion properties on the equivalence ratio has been performed. Unfortunately, results show that the real equivalence ratio in the combustion cylinder may differ significantly from the initial equivalence ratio of the mixture. This is mainly due to the oxygen already present in the combustion cylinder and that the later is left open at the top to let the exhaust products leave into the fume hood, which allows air to enter the cylinder as well. For example during a 1-min combustion of a 4kW flame at stoichiometric equivalence ratio, 46 liters of air is used. The cylinder with a diameter of 50cm and a height of 100cm already contains almost 200 liters. One could think that the inside of the flame may not be influenced by this parasite air compared to the exterior of the flame. But as opposed to an homogeneous gaseous flame, iron particles burn in an heterogeneous manner, meaning the solid fuel and the solid combustion products have very low volumetric fractions in the flame. This could lead to the oxidiser to diffuse more easily inside the center of the flame, leading to a complex equivalence ratio gradient.

In addition, adjusting the equivalence ratio also changes the velocity of the mixture leaving the nozzle, because for the same flame power, the airflow will be greater for a smaller equivalence ratio. This can also influence the combustion behavior of the particles, as it has been observed that a lower nozzle velocity disturbed the stability of the flame, as demonstrates Figure 4.2 which shows the largest turbulence of a combustion test for flames burning with different equivalence ratios. More turbulence will increase the mixing with the parasite air and may influence the combustion properties, as well as making it more difficult to observe the flame. Therefore, special carefulness must be taken into account when trying to analysis the influence of the equivalence ratio on a given combustion property of iron combustion.

As stated before, the mixture of air and iron is ignited using a pilot annular propane flame. Firstly, this propane flame will influence the gaseous content of the exhaust gases and the gas temperature. In addition, when performing several experiments, it is crucial to keep the same propane flame intensity in order to be

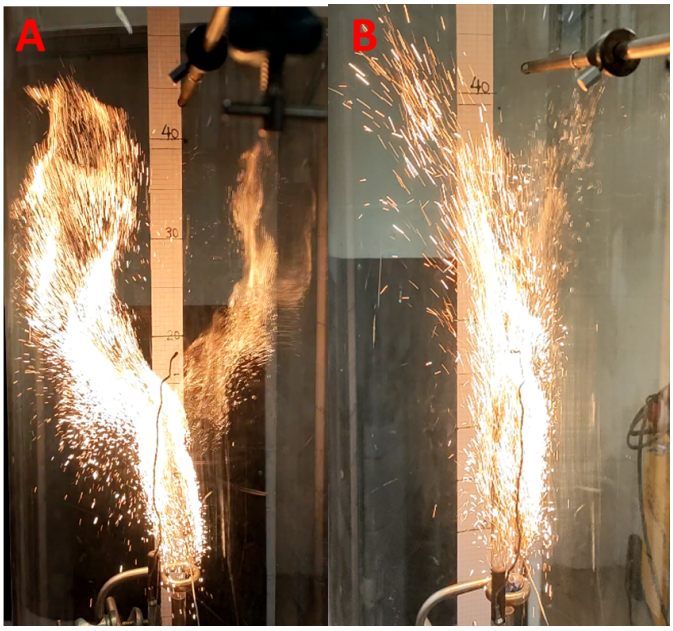

Figure 4.2: Largest turbulence of a combustion test for a flame with A) 4kW with $\phi = 1.2$, B) 4kW with $\phi = 0.6$

able to compare the results of experiments conducted under the same conditions. Indeed, as seen in the previous section, the intensity of the propane flame has a large influence on the combustion efficiency, as a flame that is not powerful enough will cause a lot of unburned particles. Unfortunately, this setup does not contain any measuring instruments capable of determining the propane flowrate. Because of this, reproducing the exact same propane flame in two different tests is a challenge.

Finally, an attempt in establishing the temperature profile of the iron flame as a function of a given input parameter was conducted. Thermocouples were used to measure the gas temperature and were placed in an axial position inside the flame. It has been observed that while the iron combustion is occurring, a deposit was formed on the tip of the probe, as can be seen in Figure 4.3. As the combustion was advancing, the deposit was getting larger which influenced the temperature measurement, as it was noticed to decrease relatively quickly. It means that when using thermocouples, the measured temperature is relevant only in the first seconds of the combustion test. Also, this deposit was not easily removable and a full shut down of the experiment was necessary to safely remove the deposit. This operation brings back the previous problem when trying to conduct several tests with the same pilot flame power. Therefore, it can be concluded that thermocouples are not suitable for relevant studies on the temperature profile as a function of an input

parameter using this setup.

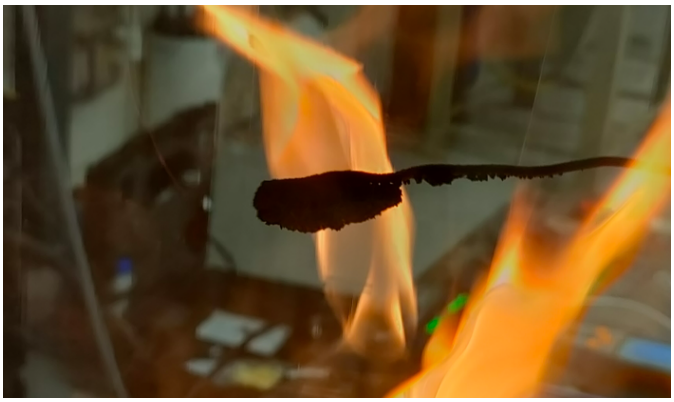

Figure 4.3: Solid deposit forming on the tip of the thermocouple as the iron combustion is occurring

4.4 Combustion efficiency of the designed burner

In order to conduct a relevant combustion experiment, it is important to know the combustion efficiency. Iron has several forms of oxidation, which are FeO, Fe_3O_4 and Fe_2O_3, respectively from the less to the most oxidised form. With a metal oxide sample recovered from the combustion, it would be possible to measure the proportion of each oxide that is contained in the sample with a X-Ray Diffraction analysis (XRD). Doing so, the efficiency of combustion can be evaluated. Indeed, with a combustion that is 100% efficient, the oxide iron sample would be composed only of Fe_2O_3. Three combustion products from combustion with different equivalence ratios were recovered by a filter situated in the fume hood, and one was recovered from falling particles at the base of the burner on a tray. An example of XRD pattern is shown in Figure 4.4 for a sample from a combustion at stoichiometric equivalence ratio. Mass fraction of iron oxides for all samples can be found in Figure 4.5.

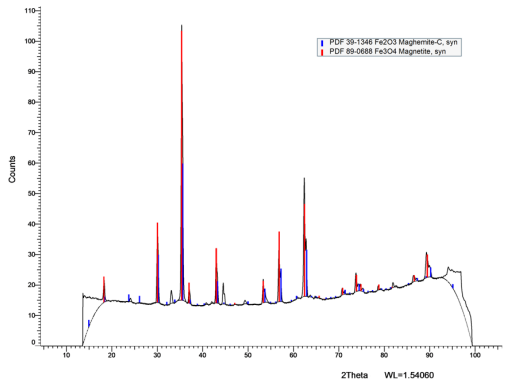

Figure 4.4: X-ray pattern of combustion products from a combustion with an equivalence ratio of 1

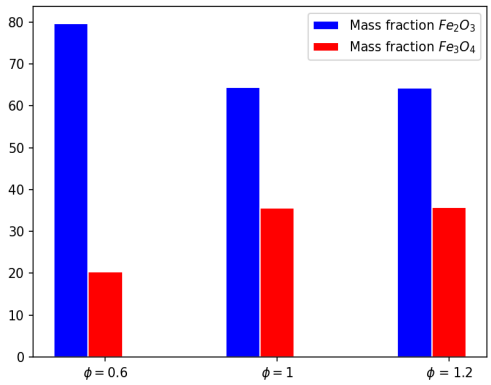

Figure 4.5: Mass composition of combustion products for combustion tests at different equivalence ratios.

For all samples, no sign of Fe and FeO were detected with the XRD analysis. A sample recovered from fallen particles at the base of the burner demonstrated the same result. It means that the burner manages to ignite all iron particles and that the oxidation is almost complete. During the oxidation, a given iron sample will increase in mass due to the addition of oxygen atoms in the products, depending on the level of oxidation. Combustion efficiency can be calculated with the mass fraction and mass gain associated to each oxide, compared to the maximal mass gain occurring for a complete oxidation. The efficiency is given by Equation 4.1 :

$$\eta = \frac{\text{mass gain sample}}{\text{mass gain max}} = \frac{w_{Fe_2O_3} \cdot g_{Fe_2O_3} + w_{Fe_3O_4} \cdot g_{Fe_3O_4}}{g_{Fe_2O_3}} \tag{4.1}$$

With $w_{Fe_2O_3}$ and $w_{Fe_3O_4}$ being the mass fractions, and $g_{Fe_3O_4} = 0,38$ and $g_{Fe_2O_3} = 0,43$ being the proportion of mass gain for each oxide relative to pure iron. We can see in Table 4.1 an oxidation efficiency of more than 96% in each case. It can be noted the slight increase in efficiency for lower mixture equivalence ratio, that could be explained by a greater availability of oxygen for the combustion as iron particles are expected to burn in the diffusion regime. It is important to keep in mind the problem of the real equivalence ratio that was explained in the previous section.

Sample	$w_{Fe_2O_3}$	$w_{Fe_3O_4}$	Combustion efficiency [%]
$\phi = 0,6$	79,7	20,3	97,7
$\phi = 1$	64,5	35,5	96,1
$\phi = 1,2$	63.8	36.2	96

Table 4.1: Mass percentage of Fe_2O_3 and Fe_3O_4 measured using XRD analysis from different combustion product samples.

4.5 Iron flame NO_x emission

It is known that combustion with oxygen often produces NO_x. An exhaust gas analyser have been employed in order to measure the NO_x emission of the burner. The system used is the *Testo 350* [65], which is a portable exhaust analysis box. Also, three thermocouples were used to measure the temperature profile of the flame. For recall, two main factors are involved in the production of NO_x, the temperature must be high enough, and oxygen must be available, as seen in section 2.2.3.4. The setup used can be seen in Figure 4.6

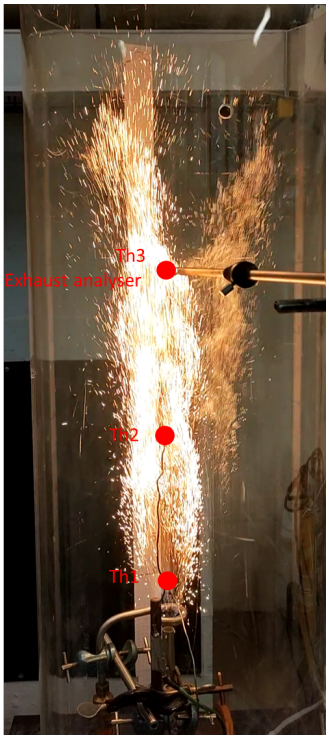

Figure 4.6: Thermocouples and exhaust analyser position.

Results on the exhaust gases emission show no sign of NO_x on the analyser.

This is in contrast to the results obtained by Winiika [19] and from the work done at Eindhoven university [26] presented in section 2.2.3.4, that demonstrated some - still very low -, NO_x emissions. One possible explanation for the non presence of NO_x concerns the temperature. Indeed, the following gas temperature were measured on the three thermocouples during the experiments, from a stoichiometric, 4kW iron flame.

	Position above propane ring [cm]	T [°C]
Thermocouple 1	5	706,6
Thermocouple 2	20	841,3
Thermocouple 3	40	346,5

Table 4.2: Temperature measured at the three thermocouples for a stoichiometric 4kW flame.

Those relatively low temperatures may be attributed to the parasite air lowering the real equivalence ratio. A lower equivalence ratio results in a lower gas flame temperature, due to the dilution of the heat in the gas, as can be seen in Figure 2.31 in section section 2.2.3.3. As the gas temperature is relatively low, the kinematic of the Zeldovich mechanism may not be fast enough to allow the formation of NO_x. Even though the gas temperature may be lower, the temperature of the metal particle itself is still near the adiabatic flame temperature at stoichiometric concentration, which is high enough as the adiabatic temperature of iron is near 2200K. Still, no NO_x was formed. One possible explanation is that the oxidation kinetics are faster than the kinetics of the Zeldovich mechanism, and thus the oxygen radicals near the particles will tend to react first with the iron particles and not with the nitrogen. Moreover, it shows that no fuel-bound and prompt NO are produced during combustion, and the the hypothesis that hydrogen also plays a significant role in the formation of NO_x, stated in section section 2.2.3.4, may be correct.

4.6 Iron flame solid products

After a combustion test of iron particles in the range 53-100μm, an oxide particle sample has been recovered using a filter situated at the entrance of the fume hood. Images of the oxide particles and raw iron powders have been obtained using a Scanning Electron Microscope (SEM), and compared on Figure 4.7. It can be seen that the oxide particles are generally larger than the corresponding fresh iron powders. This suggests that a porous solid metal oxide is formed around the

metal core of the particle, which is expected from particles burning in mode C, as explained in section section 2.2.2.2.

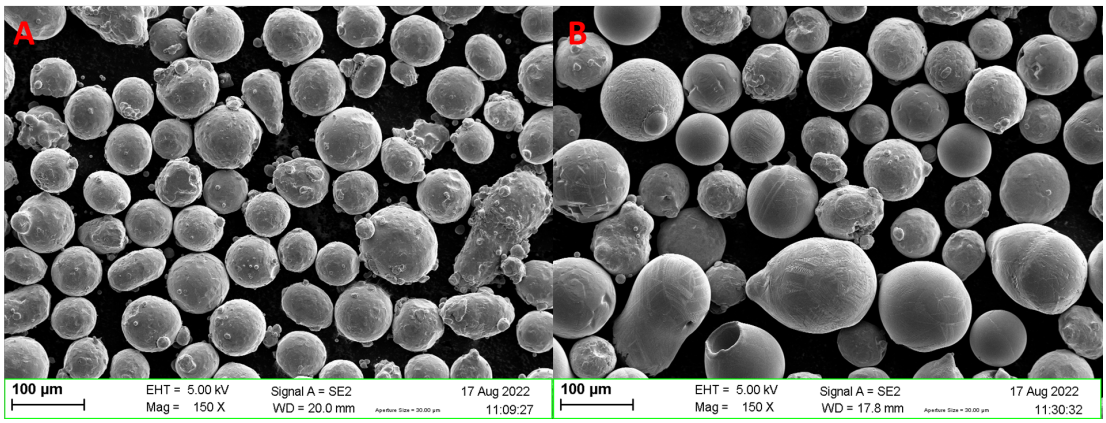

Figure 4.7: A) Fresh iron powder before combustion, B) Iron oxide powders recovered from combustion.

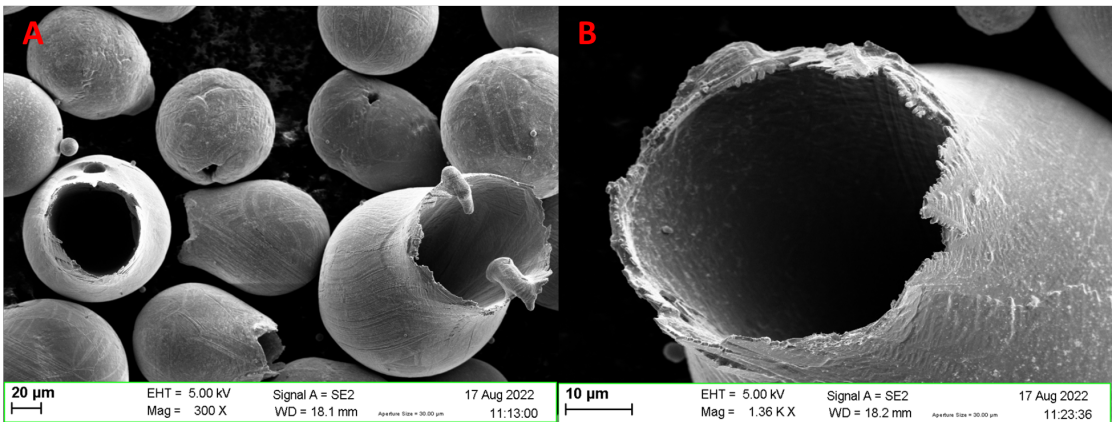

Figure 4.8: Oxide particles show cavities formed during the combustion of iron particles.

However, some particles contain holes that appear to have exploded. This could be explained by the fact that a small part of the iron particles actually evaporated from the center, causing a cavity to form which then perforated the shell due to the increasing pressure. Nevertheless there is no trace of nano oxides products in the sample. Moreover, iron oxide dentrites are visible in Figure 4.8B, which shows the solidification of molten iron oxide. The melting point of Fe_2O_3 is 1566 °C, meaning that the particle surface temperature was at least equal to that value.

However, the gas temperature have been measured to be around 800 °C, which shows that the gas temperature is significantly lower than the particle temperature. This is the trend for particles burning in a diffusion-limited regime. This validates that iron powders burn in a diffusion-limited regime, as was anticipated in section section 2.2.2.1.

4.7 Fluidization problem with smaller particle range

Two size ranges of iron particles have been tested with this burner. A 53-100μm range have been used successfully to realise the different tests described here-above. Another size range of 15-53μm have been tested before, but problems related to fluidization have been observed. Indeed, thanks to the optical access to the fluidization zone, which was covered in section section 3.3, it was possible to see that the particles had difficulty in fluidizing, to the point of almost completely blocking the air channel. The pressure than built up to the point were the entire obstruction was cleared abruptly. A large amount of iron powder was then released almost instantaneously, which could have caused serious problems in terms of security. Fortunately, the system was operating in cold mode.

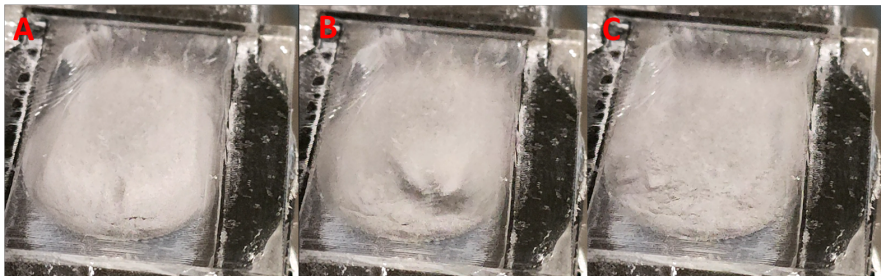

Figure 4.9: Obstruction clearance of the feeding system while using 15-53 μm iron particles. Pictures A,B and C are 3 consecutive frames from a video.

When looking at the terminal velocity for fluidizing particles in Equation 3.5, it states that the smaller range of particles should be easier to fluidize, as the terminal velocity has a $V_t \propto \sqrt{D_p}$ relationship with the particle diameter. But it is also necessary to take into account the group to which the particles belong, which are detailed in section section 3.3.1.2. Iron particles, with a density of 7,874 g/cm^3 and a range said to be between 15 to 53μm, are part mostly of the group A, while only the particles below 20μm are supposed to be in the group of particles that are difficult to fluidize, the group C. This proportion of the sample is expected to be very low and should have a small impact on the fluidization. But images of the

particles obtained using a Scanning Electron Microscope show that the proportion of particles smaller than 20μm represents the majority of the sample distribution, and that even particles smaller than 10μm are present in large numbers, as shown in Figure 4.10. SEM images show that majority of the particles are in fact part of group C. This explains why particles of this range are difficult to fluidize. Therefore, particular attention must be paid to the actual size range, and a granulometry should be performed on the sample as a precaution.

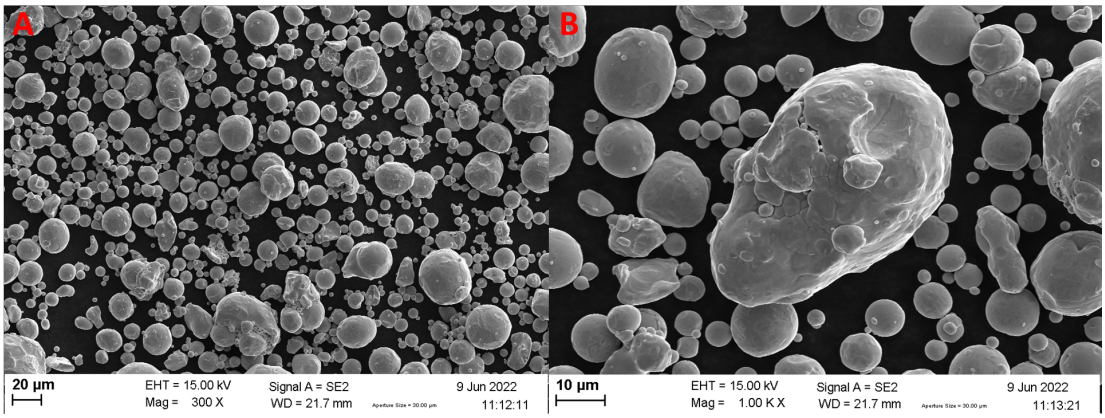

Figure 4.10: SEM images of iron particles from the 15-53μm range

Chapter 5

Conclusion

5.1 Present work

The present work introduce metal powders as an energy carrier. An introduction to the need for new Power-to-X-to-Power solutions have been presented, as well as why metal powders are good candidates, especially due to their high energy density.

A theoretical state of the art on metal powder combustion have been conducted. The main particularity of metal particles burning is that they burn heterogeneously and that, once ignited, metal particles react in individual diffusion-limited regime, forming micro-diffusion reactors that will lead to their unique appearance of flames within the flame combustion front structure. The research concerning the metal combustion is quit parse and sometime contradictory. An attempt in gathering all relevant information from those studies have been conducted, which concerns the fundamentals behind heterogeneous combustion, as well as the influence of input parameters on the combustion properties. The difficulty to compare results from different studies has been noted. Indeed, experimental setups operate in a wide range of size, from the single particle combustion to flames of several dozen kW. Each study uses an unique set of shape, size distribution, oxide content that will also influence the results. It is concluded that the state of science concerning the theory and understanding of metal powder combustion is still in its early stages and additional experimental work needs to be completed in order to validate the different models.

A setup for burning iron powder has been designed. The burner can produce a flame from 3 to 5kW while being able to modify the equivalence ratio of the mixture. A feeding system for mixing iron powder and air was 3D-modelled. It

can mix iron powder with air with a relatively good precision, having a range of variation of $\pm 7.5\%$ with a confidence level of 95%. This part of the thesis was the most troublesome part, as obtaining an efficient, constant fluidization is very challenging. Eight different iterations and more than 70 cold mode tests were necessary before obtaining the final version of the feeder. This feeding system was only effective for a larger range of particle sizes. Indeed, particles smaller than 20μm created fluidization problems due to the cohesive forces holding the particles together. After being fluidized, the mixture is transported pneumatically in a combustion chamber and is ignited using a pilot annular propane flame.

The propane flame used to ignite the particles was found to have a large influence on the quantity of unburned particles. Indeed, a flame that is not powerful enough may produce a temperature that is not sufficient for the ignition of larger particles, due to the ignition temperature increasing for larger particles in suspensions. In addition, the iron flame is not self-sustaining and requires an external heat source at all times. It has been shown that the equivalence ratio of the mixture is different to the equivalence ratio of the flame. This is mainly due to the parasite air present near the iron flame. It was hypothesized that heterogeneous combustion allows the oxidant to diffuse more easily within the flame compared to a homogeneous gaseous flame, due to the extremely low volumetric fraction of the iron fuel and the solid combustion products.

The oxide products of the combustion have been analysed, and show that the oxidation is almost complete, and that the products do not contain any unburnt particles, which validates the capacity of the feeder to efficiently burn iron particles. The combustion efficiency was found to be superior to 96%, with a negligible dependency on the mixture equivalence ratio. Analysis on the NO_x emission have been performed on the exhaust gases of the iron flame. The results showed that the flame does not produce any NO_x. This was explained by the low temperature of the flame due to a high dilution of the gas by parasite air. It also demonstrated that only the thermal mechanism is relevant in the production of NO_x. Visual analysis of combustion products from SEM images demonstrated the formation of oxide particles larger than the previous fresh iron powders, showing that an oxide shell was produced and that combustion did not occur in the vapor phase, as predicted for iron powder combustion. However, some of the particles displayed an internal cavity that may have been caused by the evaporation of a small proportion of iron in the center.

5.2 Perspectives

This first step at the UCLouvain to develop laboratory equipment to assess the combustion of metal powders in order to use them as a sustainable energy carrier, can be considered as a success. This master thesis contains important findings and highlights the difficulty of obtaining a stable heterogeneous iron flame. The results obtained in this thesis open many perspectives to continue the experimental research and make metal powders a robust and cost-effective alternative to current solutions. To do so, it would make sense to deeper investigate some critical aspects of the technology:

- In order to have relevant results while tuning the equivalence ratio, an enclosed chamber that is airtight to the surrounding must be developed.

- To perform experiments on a wider size range of particles, and ensuring a near optimal accuracy, it would be preferable to use a professional powder dispenser, at the expense of the price. Such devices can create aerosol with powders as small as 0.1 μm.

- A key aspect of the use of metal powders as energy carrier is the sustainable cycle associated. Once a closed combustion chamber is in place, the next logical step is to develop a recovery system to capture the metal oxides to be able to reduce them, thus closing the cycle, for example using a cyclone.

- Finally, as an iron flame seems to have difficulty to be self-sustaining, the use of premixed iron/hydrocarbon flame to help stabilize the flame should be investigated.

Appendix A

Initial feeder solution

A.1 Description

The final design of the first type of feeder is shown in Figure A.1. It includes directly the syringe tube inside of the cylinder. This choice was made for two reasons. Firstly because of the rough surface of the 3D print, which did not ensure the airtightness between the plunger tip of the syringe and the wall of the cylinder. Secondly, it provides a simple way to load the feeder in powder, as the syringe tube can be removed from the cylinder as needed. In order to ensure the permeability between the syringe tube and the cylinder, a O-ring joint is used in the groove shown in Figure A.3. The inner diameter of the cylinder in the upper part of the feeder fits with the inner diameter of the syringe tube so that the powder can be pushed above the tube. The powders will then meet with the air entrance of the feeder, which consists of a 0.5mm wide air knife and covers half the the cylinder perimeter. It is also inclined by 45° with respect to the horizontal as can be seen in Figure A.2, for two reasons. The first one is that the air must not fluidize particles that have not yet reach the air inlet, in order to not dig into the powder reservoir. When blowing air in an inclined manner, the inertia will make the flow go directly upward in direction of the outlet. The second reason concerns the 3D printing. Indeed, 3D printing is a layer-by-layer activity, and it requires a good foundation for the next layer to be printed correctly, with about 50% contact, which corresponds to maximum a 45° slope.

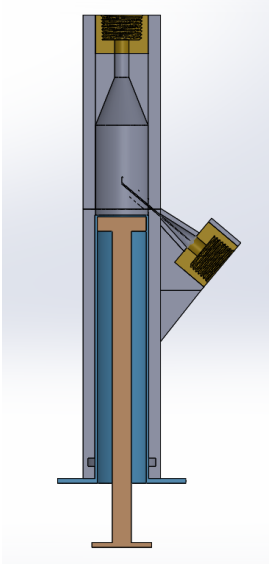

Figure A.1: Feeder

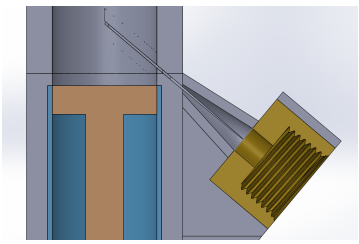

Figure A.2: Air entrance

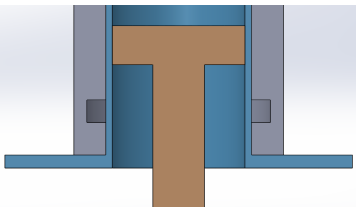

Figure A.3: O-ring

A.2 Tests

The feeding system must achieve a constant mass flowrate of powder during the whole duration of the combustion process, and this from the beginning of the experiment, which is defined as the time when the air flowrate enters the feeder and that the particles start to fluidize. For example, in a context of combustion analysis that requires a constant equivalence ratio for the full duration of the experiment, if the mass flowrate is increasing slowly at the beginning before reaching a stationary value, the equivalence ratio will not be fixed during the early stage of the combustion. It will then interfere with the results, this is especially the case if the analysis concerns the recovery of the metal oxide particles. The rate at which the particles fluidize at the start of the experiment depends mainly on the initial position of the powder in the cylinder relative to the position of the air inlet. The aim of the next experiment is to find the position of the powder at which the steady state is reached directly from the beginning of the test. For this purpose, different initial positions of the powder has been identified and shown in Figure A.4.

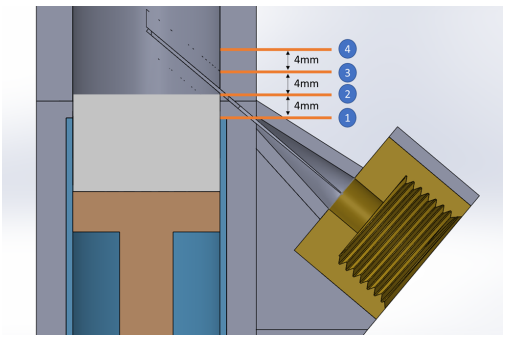

Figure A.4: Schematic representing the different initial position of the powder

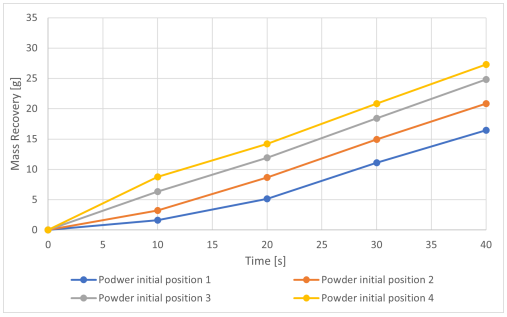

Figure A.5: Mass recovery of particle with respect to time with different initial powder position

The first position is achieved when the top of the powder is at the same height as the tip of the syringe tube. The second position corresponds to when the powders are at the same height as the air knife of the air inlet, 4mm above position 1. Position 2 and 3 are respectively 4mm and 8mm above position 2. It can be seen in Figure A.5 that the initial position 3 fits the best with a steady state mass flowrate of iron powder. This test was not conducted for the second model of feeder, because the transition time to achieve a steady state mass flowrate is very short, at about one or two seconds, which is an acceptable inaccuracy

Still in a context of doing analysis based on the tuning of the equivalence ratio. It is important to find out what is the influence of the air flowrate on the iron mass flow, with a constant stepper motor speed corresponding to a given flame power. For this experiment, measurements of the mass iron flowrate have been obtained using a cold mode setup explained in section section 3.3.4. The tests have been conducted with a power of 4kW. It can be seen in Figure A.6 that the equivalence ratio has no influence on the iron mass flowrate.

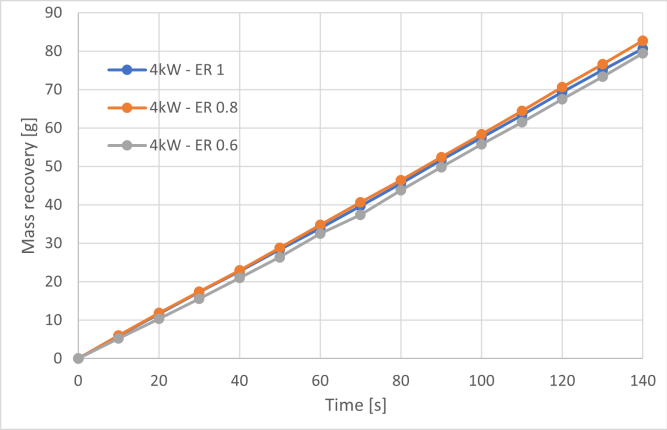

Figure A.6: Influence of air flowrate on iron mass flowrate

Appendix B

Agglomeration problem

The design process of the feeding system was the most time consuming task of the thesis. In order to evaluate the performance of a particular iteration of the feeder, more than 70 cold mode tests have been performed. During those tests, iron particles are getting fluidize in the feeder, and than go through a plastic tube in pneumatic transport before getting collected with the recovery system covered in section section 3.3.4. The iron powder stock being limited, the particles have passed through the cold mode system several times. After several re-circulation of the powders, a change in the fluidization behavior and in the appearance as been detected , as shown in Figure B.1. An optic microscope has also been used to visualise the agglomerations, as can be seen in Appendix B.

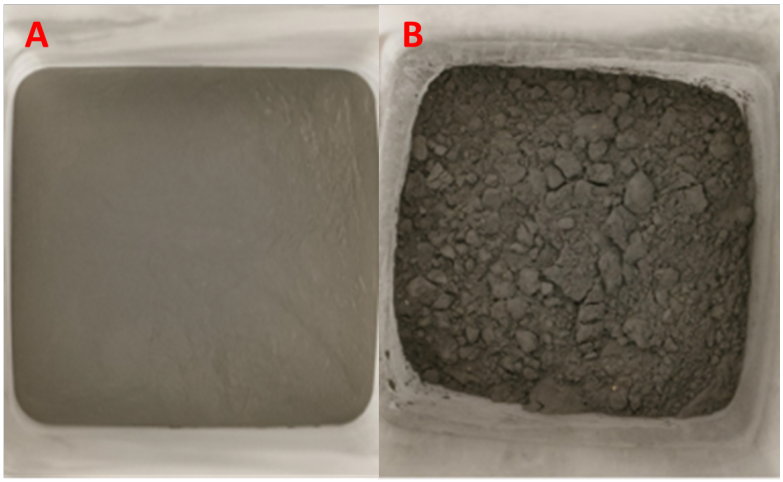

Figure B.1: A) Fresh iron powder, B) Iron powder after going several times into the cold mode system.

It is noticeable that agglomerations are formed, which poses a problem for the

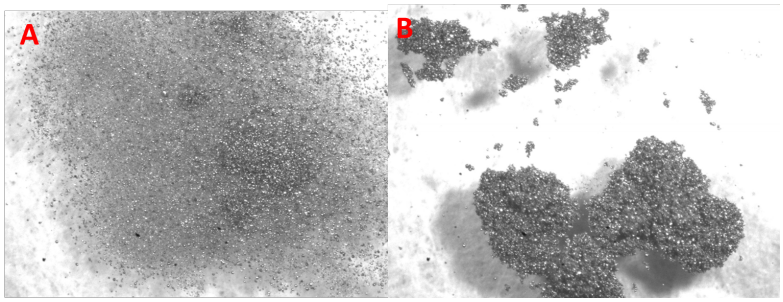

Figure B.2: Optic microscope images of A) Fresh iron powder, B) Agglomerated powder.

proper functioning of the setup. Here is a list of some of the action that were taken to identify the source of the problem:

- Sieve the powders to remove static energy : agglomerations still present.
- Leave the powders in an oven at 100°C overnight to remove moisture : agglomerations still present.
- Use of the electron microscope to check if a change has taken place in the structure/surface condition of the powders : Does not show any change in surface condition or oxidation signs.

Unfortunately, this problem have been left aside because it was outside the scope of this thesis, as only fresh powders will be used in real applications.

Appendix C

Filter Selection Chart

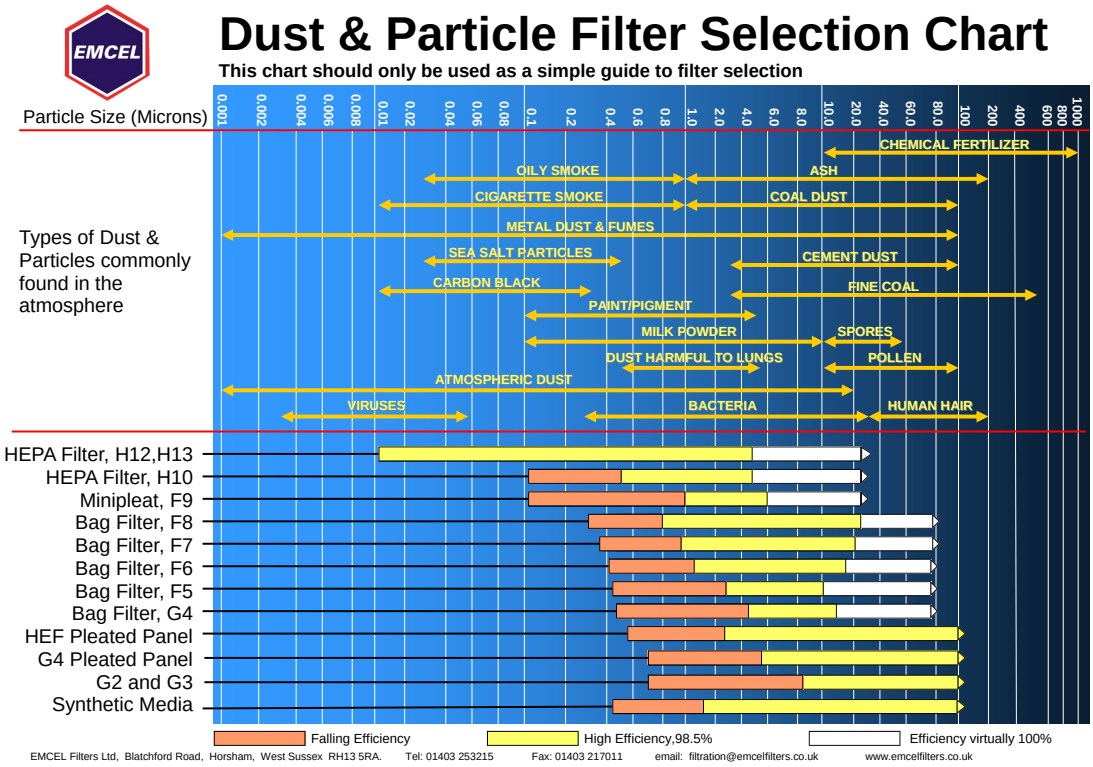

Figure C.1: Particle filter selection guide [66].

Bibliography

[1] Environmental Institute and Energy Study. Fossil fuels. 2021.

[2] Thirugnanasambandam Mirunalini, S. Iniyan, and Goic Ranko. A review of solar thermal technologies. *Renewable and Sustainable Energy Reviews*, 14(1):312–322, 2010.

[3] G. Lambert Jessica, A. S. Hall Charles, Balogh Stephen, Gupta Ajay, and Arnold Michelle. Energy, eroi and quality of life. *Energy Policy*, 64:153–167, 2014.

[4] US. Energy Information Administration. International energy outlook 2021. *EIA*, 2021.

[5] United Nations. Paris agreement. 2015.

[6] Carlos, Carpintero Óscar, Frechoso Fernando, Mediavilla Margarita, and J. Luis. A top-down approach to assess physical and ecological limits of biofuels. *Energy*, 64:506–512, 2014.

[7] International Energy Agency (I.E.A.). Net zero by 2050, a roadmap for the global energy sector. 2021.

[8] Ting Yang, Yingjie Zhao, Haibo Pen, and Zhaoxia Wang. Data center holistic demand response algorithm to smooth microgrid tie-line power fluctuation. *Applied Energy*, 231:277–287, 2018.

[9] Frits Møller Andersen, Mattia Baldini, Lars Gårn Hansen, and Carsten Lynge Jensen. Households' hourly electricity consumption and peak demand in denmark. *Applied Energy*, 208:607–619, 2017.

[10] Hwang Hyun Tae and Varma Arvind. Hydrogen storage for fuel cell vehicles. *Current Opinion in Chemical Engineering*, 5:42–48, 2014.

[11] J. M. Bergthorson, S. Goroshin, M. J. Soo, P. Julien, J. Palecka, D. L. Frost, and D. J. Jarvis. Direct combustion of recyclable metal fuels for zero-carbon heat and power. *Applied Energy*, 160:368–382, 2015.

[12] M. Bergthorson Jeffrey. Recyclable metal fuels for clean and compact zero-carbon power. *Progress in Energy and Combustion Science*, 68:169–196, 2018.

[13] Soo Michael, Mi Xiaocheng, Goroshin Samuel, J. Higgins Andrew, and M. Bergthorson Jeffrey. Combustion of particles, agglomerates, and suspensions – a basic thermophysical analysis. *Combustion and Flame*, 192:384–400, 2018.

[14] Philippe Julien and Jeffrey M. Bergthorson. Enabling the metal fuel economy: green recycling of metal fuels. *Sustainable Energy amp; Fuels*, 1(3):615–625, 2017.

[15] K. A. Trowell, S. Goroshin, D. L. Frost, and J. M. Bergthorson. Aluminum and its role as a recyclable, sustainable carrier of renewable energy. *Applied Energy*, 275:115112, 2020.

[16] Yavor Yinon, Goroshin Sam, M. Bergthorson Jeffrey, and L. Frost David. Comparative reactivity of industrial metal powders with water for hydrogen production. *International Journal of Hydrogen Energy*, 40(2):1026–1036, 2015.

[17] D. Ning, Y. Shoshin, J.A. Van Oijen, G. Finotello, and L.P.H. De Goey. Burn time and combustion regime of laser-ignited single iron particle. *Combustion and Flame*, 230:111424, 2021.

[18] Pál Tóth, Yngve Ögren, Alexey Sepman, Per Gren, and Henrik Wiinikka. Combustion behavior of pulverized sponge iron as a recyclable electrofuel. *Powder Technology*, 373:210–219, 2020.

[19] Henrik Wiinikka, Therese Vikström, Jonas Wennebro, Pal Toth, and Alexey Sepman. Pulverized sponge iron, a zero-carbon and clean substitute for fossil coal in energy applications. *Energy Fuels*, 32(9):9982–9989, 2018.

[20] 2022.

[21] Sun Jin-Hua, Dobashi Ritsu, and Hirano Toshisuke. Structure of flames propagating through metal particle clouds and behavior of particles. *Symposium (International) on Combustion*, 27(2):2405–2411, 1998.

[22] Tang François-David, Goroshin Samuel, and J. Higgins Andrew. Modes of particle combustion in iron dust flames. *Proceedings of the Combustion Institute*, 33(2):1975–1982, 2011.

[23] R. Saidur, E. A. Abdelaziz, A. Demirbas, M. S. Hossain, and S. Mekhilef. A review on biomass as a fuel for boilers. *Renewable and Sustainable Energy Reviews*, 15(5):2262–2289, 2011.

[24] *Key World Energy Statistics 2016*. 2016.

[25] Clark Richard, Zucker Noah, and Urpelainen Johannes. The future of coal-fired power generation in southeast asia. *Renewable and Sustainable Energy Reviews*, 121:109650, 2020.

[26] Eindhoven University of Technology Nederland Maritiem Land. Ijzer als brandstof voor schepen (iron as fuel for ships). 2019.

[27] TeamSolid, 2020.

[28] Team Solid. Metal power, 2020.

[29] Goroshin Samuel, Palečka Jan, and M. Bergthorson Jeffrey. Some fundamental aspects of laminar flames in nonvolatile solid fuel suspensions. *Progress in Energy and Combustion Science*, 91:100994, 2022.

[30] SOLID. World's first iron-based energy storage system. 2019.

[31] Driss Laraqui, Gontrand Leyssens, Cornelius Schonnenbeck, Olivier Allgaier, Ricardo Lomba, Clément Dumand, and Jean-François Brilhac. Heat recovery and metal oxide particles trapping in a power generation system using a swirl-stabilized metal-air burner. *Applied Energy*, 264:114691, 2020.

[32] Michelle McRae, Philippe Julien, Santino Salvo, Samuel Goroshin, David L Frost, and Jeffrey M Stabilized, flat iron flames on a hot counterflow burner. 37(3):3185–3191, 2019.

[33] Jan Palečka, Jessica Sniatowsky, Samuel Goroshin, Andrew J. Higgins, and Jeffrey M. Bergthorson. A new kind of flame: Observation of the discrete flame propagation regime in iron particle suspensions in microgravity. *Combustion and Flame*, 209:180–186, 2019.

[34] R. Lomba, P. Laboureur, C. Dumand, C. Chauveau, and F. Halter. Determination of aluminum-air burning velocities using piv and laser sheet tomography. *Proceedings of the Combustion Institute*, 37(3):3143–3150, 2019.

[35] A. Williams, M. Pourkashanian, J. M. Jones, and N. Skorupska. Combustion and gasification of coal. 2018.

[36] Prabir Basu. Combustion and gasification in fluidized beds.

[37] David Albertovich Frank-Kamenetskii. *Diffusion and heat exchange in chemical kinetics*, volume 2171. Princeton University Press, 2015.

[38] Lev Abramovich Vulis. *Thermal regimes of combustion*. McGraw-Hill, 1961.

[39] Nikolai Nikolaevic Semenov. Chain reactions. *Goshimizdat*, 1934.

[40] Xiaocheng Mi; Aki Fujinawa; Jeffrey M. Bergthorson. A quantitative analysis of the ignition characteristics of fine iron particles. *arXiv pre-print server*, 2021.

[41] V. I. Bolobov. *Combustion, Explosion, and Shock Waves*, 37(3):292–296, 2001.

[42] A. V. Grosse and J. B. Conway. Combustion of metals in oxygen. *Industrial Engineering Chemistry*, 50(4):663–672, 1958.

[43] T. Hazenberg and J. A. Van Oijen. Structures and burning velocities of flames in iron aerosols. *Proceedings of the Combustion Institute*, 38(3):4383–4390, 2021.

[44] Irvin Glassman, Richard A Yetter, and Nick G Glumac. *Combustion*. Academic press, 2014.

[45] Jinhua Sun, Ritsu Dobashi, and Toshisuke Hirano. Combustion behavior of iron particles suspended in air. *Combustion Science and Technology - COMBUST SCI TECHNOL*, 150:99–114, 1990.

[46] S. Nelson Lloyd, E. Rosner Daniel, C. Kurzius Shelby, and S. Levine Herman. Combustion of zirconium droplets in oxygen/rare gas mixtures—kinetics and mechanism. *Symposium (International) on Combustion*, 12(1):59–70, 1969.

[47] Bernard Lewis and Guenther Von Elbe. *Combustion, flames and explosions of gases*. Elsevier, 2012.

[48] Chung K Law. *Combustion physics*. Cambridge university press, 2010.

[49] Michael J. Soo, Keishi Kumashiro, Samuel Goroshin, David L. Frost, and Jeffrey M. Bergthorson. Thermal structure and burning velocity of flames in non-volatile fuel suspensions. *Proceedings of the Combustion Institute*, 36(2):2351–2358, 2017.

[50] Hans M Cassel. *Some fundamental aspects of dust flames*, volume 6551. US Department of the Interior, Bureau of Mines, 1964.

[51] D. R. Ballal. Flame propagation through dust clouds of carbon, coal, aluminium and magnesium in an environment of zero gravity. *Proceedings of the Royal Society of London. Series A, Mathematical and Physical Sciences*, 385(1788):21–51, 1983.

[52] S. Goroshin, I. Fomenko, and J. H. S. Lee. Burning velocities in fuel-rich aluminum dust clouds. *Symposium (International) on Combustion*, 26(2):1961–1967, 1996.

[53] Ning Daoguan, Shoshin Yuriy, Martijn, Jeroen, Finotello Giulia, and Philip. Temperature and phase transitions of laser-ignited single iron particle. *Combustion and Flame*, 236:111801, 2022.

[54] J. Warnatz, U. Maas, and R.W. Dibble. *Combustion: Physical and Chemical Fundamentals, Modeling and Simulation, Experiments, Pollutant Formation.* Springer Berlin Heidelberg, 2012.

[55] Hervé Jeanmart Francesco Contino. Lmeca2220 internal combustion engines. 2021.

[56] Patxi Garra, Gontrand Leyssens, Olivier Allgaier, Cornelius Schönnenbeck, Valérie Tschamber, Jean-François Brilhac, Toni Tahtouh, Olivier Guézet, and Sylvain Allano. Magnesium/air combustion at pilot scale and subsequent pm and no x emissions. *Applied Energy*, 189:578–587, 2017.

[57] Driss Laraqui, Olivier Allgaier, Cornelius Schönnenbeck, Gontrand Leyssens, Jean-François Brilhac, Ricardo Lomba, Clément Dumand, and Olivier Guézet. Experimental study of a confined premixed metal combustor: Metal flame stabilization dynamics and nitrogen oxides production. *Proceedings of the Combustion Institute*, 37(3):3175–3184, 2019.

[58] D. Geldart. Types of gas fluidization. *Powder Technology*, 7(5):285–292, 1973.

[59] Zhou Tao and Li Hongzhong. Force balance modelling for agglomerating fluidization of cohesive particles. *Powder Technology*, 111(1):60–65, 2000.

[60] PALAS. Beg 1000.

[61] CNRS. Solar fuel | cnrs in english. 2020.

[62] Hao Li, Hong Li, Xiuqiao Huang, Qibiao Han, Ye Yuan, and Bin Qi. Numerical and experimental study on the internal flow of the venturi injector. *Processes*, 8(1):64, 2020.

[63] Michael Soo, Philippe Julien, Samuel Goroshin, Jeffrey Bergthorson, and David Frost. Stabilized flames in hybrid aluminum-methane-air mixtures. *Proceedings of the Symposium on Combustion*, 34, 2013.

[64] M. Sadik. Air pollution and control.

[65] Testo. Testo 350 - analysis box for exhaust gas analysis systems.

[66] EMCEL. Dust particle filter selection chart. 2022.

UNIVERSITÉ CATHOLIQUE DE LOUVAIN
École polytechnique de Louvain
Rue Archimède, 1 bte L6.11.01, 1348 Louvain-la-Neuve, Belgique | **www.uclouvain.be/epl**